MISSIONE 4
ISTRUZIONE
RICERCA

National Recovery and Resilience Plan (NRRP)
Mission 4, Component 2 (M4C2) – Investment 1.1: Fund for the National Research Programme (NRP) and Research Projects of Significant National Relevance (PRIN)
Call PRIN 2022 PNRR – Directorial Decree no.1409, 14/09/2022

Enhancing our understanding of Subsidence RISK induced by groundwater exploitation towards sustainable urban development

CUP: B53D23033400001

DEL 6.3

Future land subsidence risk in the metropolitan cities of Italy

Authors: R. Paranunzio, F. Cigna (CNR-ISAC), R. Bonì (IUSS), P. Teatini (UNIPD)

Version 1.0, Issue date: 28/02/2026

Dissemination level: Public

Finanziato dall'Unione europea NextGenerationEU | Ministero dell'Università e della Ricerca | Italiadomani | CNR ISAC | IUSS Scuola Universitaria Superiore Pavia | Università degli Studi di Padova

How to cite this document

PARANUNZIO R., CIGNA F., BONÌ R. & TEATINI P. (2026). *PRIN 2022 PNRR SubRISK+ Deliverable DEL 6.3: Future land subsidence risk in the metropolitan cities of Italy*, Version 1.0, Issue date: 28/02/2026, pp. 36. Public Report. Available at: www.subrisk.eu/deliverables/

Acknowledgements

The authors would like to thank Dr C. Zoccarato at the University of Padua for the fruitful discussions on building vulnerability to land subsidence and differential displacement.

Revision history

Revision no.	*Authors*	*Date*	*Description*
1.0	PARANUNZIO R., CIGNA F., BONÌ R. & TEATINI P.	28/02/26	First release

Executive summary

This report summarizes the results of SubRISK+ Work Package (WP) n.6 (*WP6: Future land subsidence risk in the metropolitan cities of Italy*), aimed to develop a methodology to assess future scenarios of land subsidence risk at the national scale based on climate data in-situ observations and projections, satellite-derived ground displacement observations, urban settlements and land cover data, and groundwater withdrawals. Specifically, the methodology exploits: climate data from E-OBS daily gridded meteorological data and CORDEX Regional Climate Models (RCM) simulations for the European domain (EURO-CORDEX), interferometric radar datasets from the European Ground Motion Service (EGMS) of the Copernicus Programme, along with urban settlement characteristics from the Global Human Settlement Layer (GHSL) and World Settlement Footprint (WSF) datasets, land cover change information from CORINE Land Cover (CLC), Open Street Maps (OSM) datasets and groundwater withdrawals from the Italian National Institute of Statistics (Istat). These are used to estimate the future distribution and levels of hazard and exposure-vulnerability across the 15 metropolitan cities of Italy in 2050 and 2100 and, in turn, classify and map risk levels.

Projected subsidence patterns under RCP 4.5 and 8.5 indicate a clear shift toward higher hazard levels in Italian metropolitan areas by 2100, with substantial growth of high (H3) and very high (H4) hazard zones. Exposure–Vulnerability (EV) remains dominated by high and very high classes (EV3–EV4), reflecting dense, aging, and structurally fragile urban fabrics. As a result, Medium Risk (R2) prevails across all cities, while High Risk (R3) areas expand markedly reaching up to 40% in some metropolitan regions by the end of the century. These trends highlight increasing susceptibility of urban systems to climate-driven subsidence impacts.

The generated maps [DEL6.1] provide a risk assessment overview across the 2050s and 2100s for the 15 metropolitan cities in relation to the process of vertical differential displacement induced by land subsidence/uplift, taking into account anthropic (water withdrawal) and climatic factors. The approach underneath is graphically summarized in DEL6.2 and detailed in this report ([DEL6.3]).

Table of contents

1 INTRODUCTION

SubRISK+: Enhancing our understanding of Subsidence RISK induced by groundwater exploitation towards sustainable urban development is a collaborative research project funded in 2023–2026 in the framework of the Italian National Recovery and Resilience Plan (NRRP), Mission 4, Component 2 (M4C2) – Investment 1.1: Fund for the National Research Programme (NRP) and Research Projects of Significant National Relevance (PRIN) [Call "PRIN 2022 PNRR", D.D. no.1409, 14/09/2022], and led by the National Research Council (CNR) of Italy – Institute of Atmospheric Sciences and Climate (ISAC), in collaboration with the University School for Advanced Studies (IUSS) of Pavia – Department of Science, Technology and Society (STS), and the University of Padua (UNIPD) – Department of Civil, Environmental and Architectural Engineering (ICEA).

This report summarizes the results of SubRISK+ Work Package (WP) n.6 (*WP6: Future scenarios analysis*), aimed to develop a methodology to assess future land subsidence risk at the national scale based on satellite-derived ground displacement observations, demographic, groundwater and land cover data, and climate projections. Section 2 describes the used input datasets (section 2.1) and the developed risk assessment methodology (section 2.2). Future scenarios results are then presented in section 3, which provides: example of model calibration for Bologna metropolitan area (section 3.1), statistics on future hazard, exposure-vulnerability and risk for the 15 metropolitan cities of Italy as a whole, as well as city-specific mapping of hazard, exposure-vulnerability and resulting risk zoning (section 3.2 and 3.3).

The digital version of the future hazard, exposure-vulnerability and risk maps for the 15 metropolitan cities is available through SubRISK+ project website within the '*Control Room*' (https://controlroom.subrisk.eu), which enables open access to SubRISK+ mapping products.

2 DATA & METHODS

2.1 Input datasets

The input datasets of the analysis include: i) administrative boundaries and population data, ii) ground displacement observations derived from satellite radar data; iii) E-OBS daily gridded meteorological data and CORDEX regional climate models (RCM) simulations for the European domain (EURO-CORDEX); iv) land cover and urban settlements datasets; v) groundwater withdrawals from the Italian National Institute of Statistics (Istat).

Each dataset and its main characteristics are described in the following sections.

2.1.1 Administrative boundaries and population

The administrative boundaries for the 15 metropolitan cities of Italy (Figure 1) were obtained from the National Institute of Statistics (Istat; https://www.istat.it/en), the official provider of statistical data in Italy. Istat annually releases updated digital boundary datasets for Italian municipalities, provinces, and regions, along with unique identification codes that facilitate linkage with census data and other official statistical records.

The 2025 version of the geographical database was exploited for the analysis, in its GIS-ready vector format (shapefile), with WGS84 / UTM zone 32N (EPSG:32632) projected coordinates. For each metropolitan city, the dataset includes several attributes, among which are COD_REG (the unique regional identifier), COD_PROV (the unique provincial identifier), and COD_CM (the unique identifier of the metropolitan city). At the municipal level, the dataset provides these identifiers as well as additional attributes, including PRO_COM (the unique municipal code) and COMUNE (the municipality name). Table 1 summarizes the total area and the number of municipalities within each metropolitan city, together with the recorded population as of 2024 as in the last Istat census.

Table 1 – Information on the 15 metropolitan cities of Italy: area, number of towns and inhabitants according to the 2024 census.

COD_REG	*Region*	*COD_CM*	*Metropolitan City*	*Area [km²]*	*No. of towns*	*Inhabitants*
1	Piemonte	201	**Torino**	6,827	312	2,204,276
7	Liguria	210	**Genova**	1,834	67	818,812
3	Lombardia	215	**Milano**	1,575	133	3,246,455
5	Veneto	227	**Venezia**	2,473	44	834,306
8	Emilia-Romagna	237	**Bologna**	3,702	55	1,017,536
9	Toscana	248	**Firenze**	3,514	41	988,068
12	Lazio	258	**Roma**	5,363	121	4,222,648
15	Campania	263	**Napoli**	1,179	92	2,963,633
16	Puglia	272	**Bari**	3,863	41	1,219,545
18	Calabria	280	**Reggio Calabria**	3,210	97	512,956
19	Sicilia	282	**Palermo**	5,009	82	1,200,957
		283	**Messina**	3,266	108	596,147
		287	**Catania**	3,574	58	1,070,169
20	Sardegna	290	**Sassari**	4,286	66	471,957
		292	**Cagliari**	4,309	70	417,532

2.1.2 Ground displacement observations

Satellite-based ground displacement measurements were obtained from the Copernicus European Ground Motion Service (EGMS). This service delivers millimetre-level displacement estimates derived from multi-temporal Interferometric Synthetic Aperture Radar (InSAR) processing of Copernicus Sentinel-1 radar data. The products are updated annually and are openly accessible to users.

For this study, the EGMS Ortho 2018–2022 vector datasets were used, which represent point-based layers of ground displacement estimates in the vertical and east–west directions (Figure 1). They are generated by combining data from ascending and descending satellite orbits within the EGMS Calibrated datasets, which provide line-of-sight measurements referenced to a model based on global navigation satellite system data. The Ortho products are resampled onto a 100 m grid and distributed in both raster (GeoTIFF) and vector (CSV) formats. Each point includes an associated displacement time series, with temporal sampling corresponding to the satellite revisit interval (6 or 12 days).

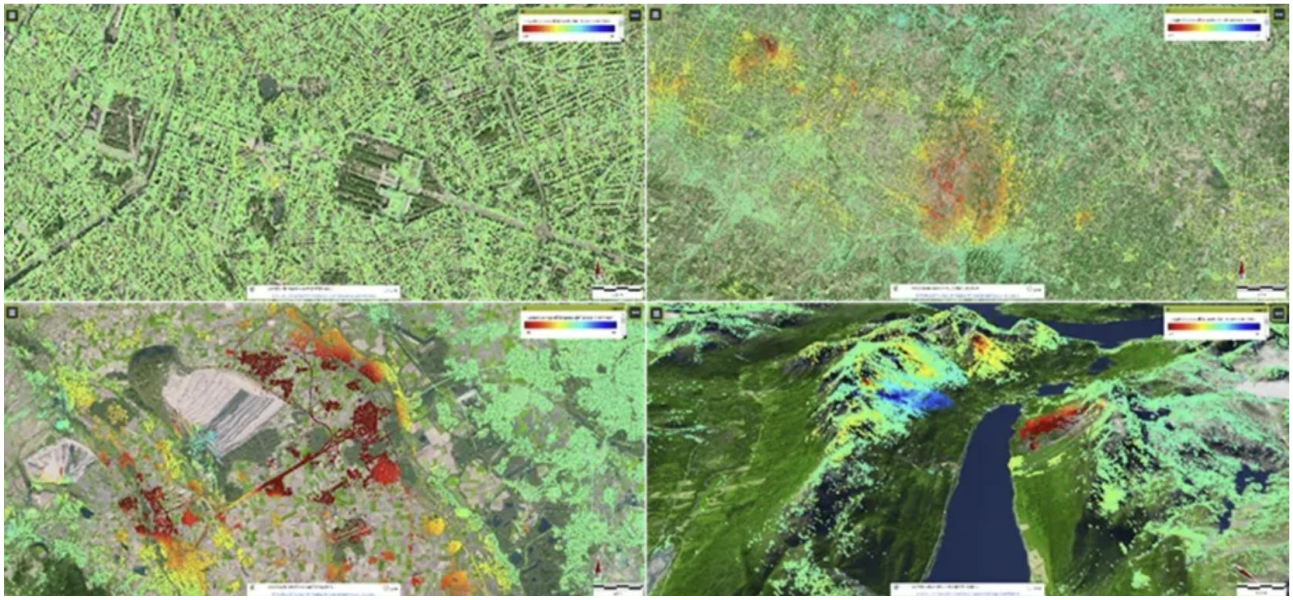

Figure 1 Example of ground motion examples from EGMS (source: https://land.copernicus.eu/en/products/european-ground-motion-service?tab=technical_summary)

2.1.3 Climate data

2.1.3.1 E-OBS

Station data derive from the European National Meteorological and Hydrological Services (NMHSs) or other data holding institutions. E-OBS is a daily gridded land-only observational dataset, specifically developed for Europe within the framework of the European Union Sixth Framework Programme ENSEMBLES project (van der Linden and Mitchell 2009). The dataset is freely available

under an open licence through the Copernicus Climate Data Store (CDS) (https://cds.climate.copernicus.eu/). It provides daily gridded observations of precipitation, temperature, and sea level pressure. The underlying station data, quality-controlled and supplied by national meteorological services, were compiled under the European Climate Assessment & Dataset (ECA&D) initiative. Air temperature fields in E-OBS are generated by interpolating station measurements and are delivered as an ensemble of equally likely realizations. In this study, the ensemble mean is used, representing the best available estimate of the selected variable.

The complete dataset extends back to 1950 and is provided on a regular 0.1° grid. It currently incorporates data from approximately 3,700 temperature stations, offering a higher station density than other gridded products derived from National Meteorological and Hydrological Services (Cornes et al. 2018). However, the number of stations contributing to each grid cell varies spatially across Europe. Owing to its spatial resolution, daily temporal granularity, and long-term coverage, E-OBS is considered a state-of-the-art gridded temperature dataset for Europe and is particularly well suited for climate impact assessments such as this study. Here, daily mean, minimum, and maximum air temperatures are analysed. For multi-day periods, mean, minimum, and maximum temperatures are calculated as the average of the corresponding daily values.

2.1.3.2 EURO-CORDEX

EURO-CORDEX is the European branch of the international CORDEX (Coordinated Regional Climate Downscaling Experiment) initiative (Jacob et al. 2014), coordinated under the World Climate Research Programme (WCRP). It provides regional climate projections of many climate variables for Europe at grid resolutions of about 0.44° (~50 km) and 0.11° (~12.5 km), applying an ensemble of Regional Climate Models (RCMs) in their most recent versions, driven by the latest Global Climate Models (GCMs) projections.

Historical simulations are available from 1950 onward under different Representative Concentration Pathways (RCPs) emission scenarios. EURO-CORDEX simulations are commonly accessed through the Copernicus Climate Change Service (C3S) Climate Data Store or the ESGF (Earth System Grid Federation), typically provided in NetCDF format. It represents one of the main sources of high-resolution climate projections for Europe, widely used in climate impact and adaptation research.

In this work, daily mean, max and min temperature and total precipitation data at 12 km spatial resolution over the temporal horizon 2023–2100, exploiting RCP4.5 and 8.5 (Jacob et al. 2014). Specifically, we used four RCMs nested within three GCMs (Table 1).

Table 1 RCMs nested into GCMs selected for this work

RCM	***GCM***		
	CNRM-CM5	ICHEC- EC-EARTH	MPI-ESM-LR
HIRHAM5		X	
RACMO22E		X	
RCA4	X	X	X
CCLM4-8-17		X	X

2.1.4 Land cover and urban settlement datasets

Several land cover and urban settlement datasets were exploited, as listed below.

2.1.4.1 Global Human Settlement Layers (GHSL)

The Global Human Settlement Layer (GHSL) is a global spatial dataset that maps the evolution and distribution of human settlements on Earth (Figure 2). It is developed by the European Commission through its Joint Research Centre (JRC). It includes a suite of products derived from satellite imagery and census data. Specifically for this work, two datasets were used: i) the Settlement Characteristics GHS-BUILT-S R2023A dataset; ii) the Settlement Characteristics GHS-BUILT-C R2023A dataset, derived from a composite of Copernicus Sentinel-2 2018 imagery and other GHS R2023A data. GHS-BUILT-S dataset represents the distribution of built-up areas, measured in square metres. It provides information on both the total built-up surface and the portion designated for predominant non-residential (NRES) uses. These data are spatially and temporally interpolated or extrapolated at five-year intervals from 1975 to 2030 at a 100 m resolution. For the reference year 2018, the dataset is available at a 10 m spatial resolution, based on observations derived from Sentinel-2 imagery. GHSL-BUILT-C delineates the boundaries of the human settlements and identifies their inner characteristics in terms of the morphology of the built environment and the functional use: built spaces (residential and non-residential, with associated height class) and open spaces (water surfaces, low to high vegetation surfaces, and roads) are distinguished within the human settlements (while the remainder is classified as no data). This layer is openly available in raster format with 10 m spatial resolution, in the World Mollweide (EPSG:54009) projected system.

2.1.4.2 World Settlement Footprint (WSF)

The World Settlement Footprint (WSF) Evolution dataset (https://geoservice.dlr.de/web/maps/eoc:wsfevolution) is produced through the analysis of Landsat-5 and Landsat-7 imagery, including derived spectral indices and temporal statistical metrics. It provides annual delineations of settlement and non-settlement areas from 1985 to 2015 (Figure 3). The dataset is openly accessible in raster format at a spatial resolution of 30 meters and is referenced to the WGS84 (EPSG:4326) geographic coordinate system.

2.1.4.3 Land cover, elevation and structural/infrastructural constraints

Copernicus CORINE Land Cover (CLC) data (https://land.copernicus.eu/en) for the reference year 2018 has been used. It provides 44 thematic classes for the 2018 reference year (Figure 4). The dataset includes 44 thematic classes for the reference year 2018. It has a Minimum Mapping Unit (MMU) of 25 ha for areal features and a Minimum Mapping Width (MMW) of 100 m for linear features. The data are provided in both vector format and as a 100 m resolution raster.

To better investigate structural and infrastructural constraints to urban expansion, data from Open Street Map (OSM) data have been used, in particular rail and road network and buildings. Data are available in vectorial format. These act as accurate indicators of urban presence by delineating built-up environments. They are available through OSM server in QGIS or Geofabrik website (http://download.geofabrik.de/openstreetmap/).

For elevation and slope information of the Italian territory, we relied on TINITALY/1.1 DEM (Figure 5) provided by the Italian National Institute of Geophysics and Volcanology (https://tinitaly.pi.ingv.it/). This DEM was obtained starting from separate DEMs of single administrative regions of Italy. The DEM is freely available as a 10 m-cell size grid (in GeoTIFF format), in the UTM WGS 84 zone 32 projection system (Tarquini et al. 2012).

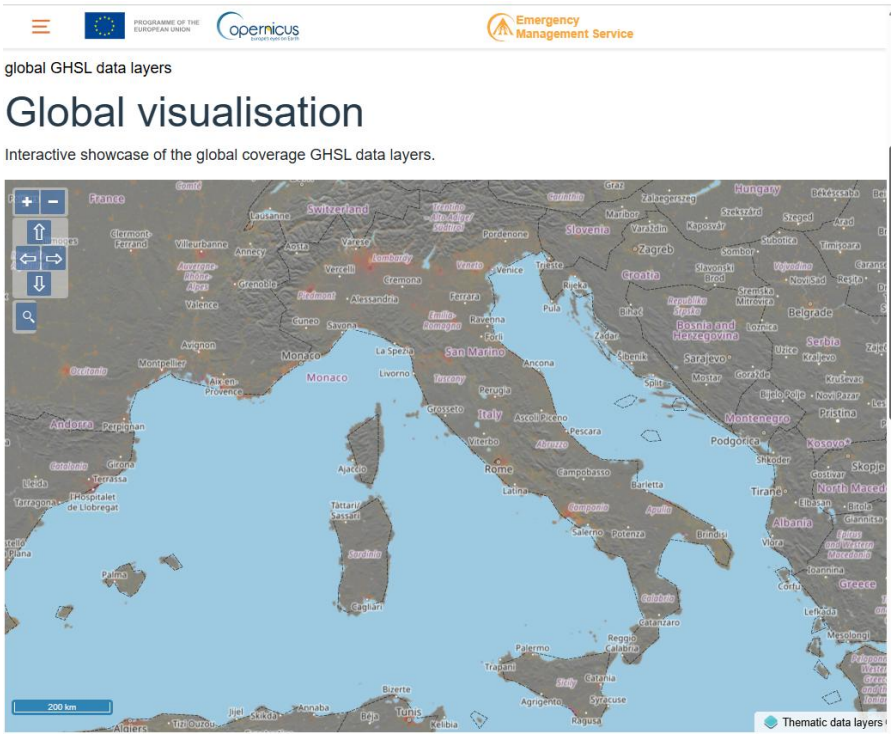

Figure 2 Overview of the GHSL data layers coverage over Italy (https://human-settlement.emergency.copernicus.eu/index_op.php).

Figure 3 Overview of the World Settlement Footprint (WSF) Evolution dataset over Italy (https://geoservice.dlr.de/web/maps/eoc:wsfevolution).

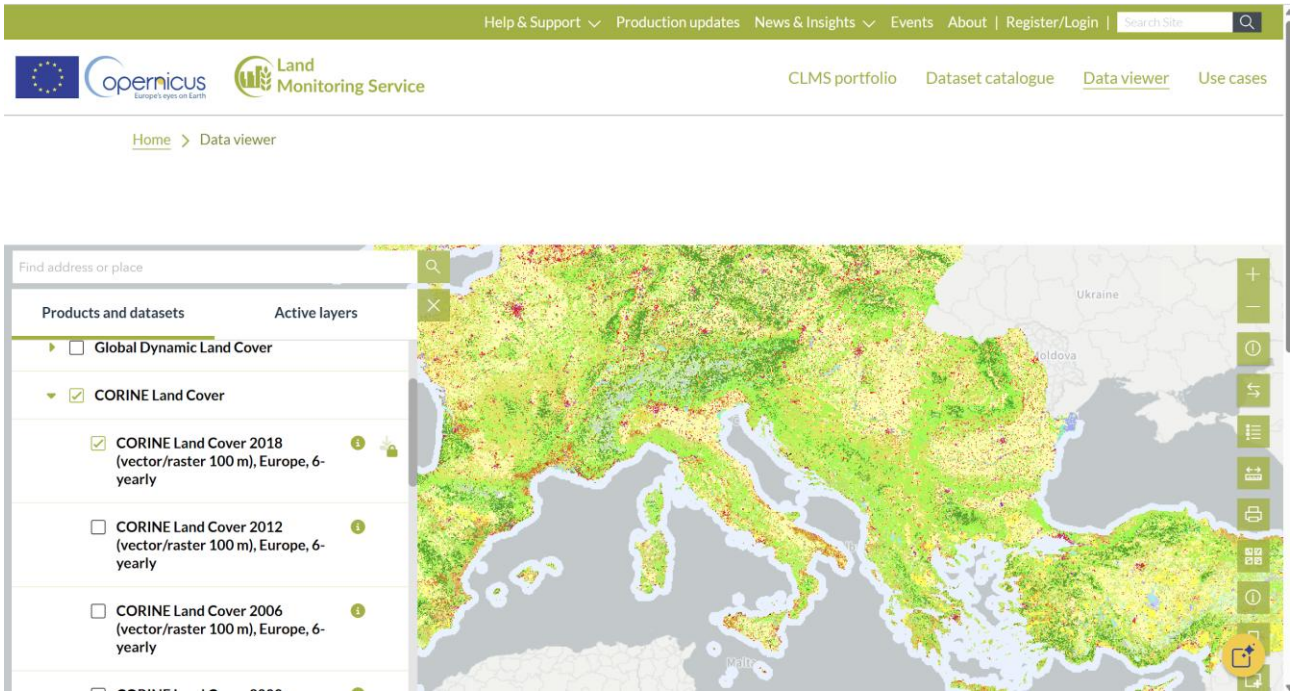

Figure 4 Overview of CORINE Land Cover data (https://land.copernicus.eu/en/products/corine-land-cover/clc2018).

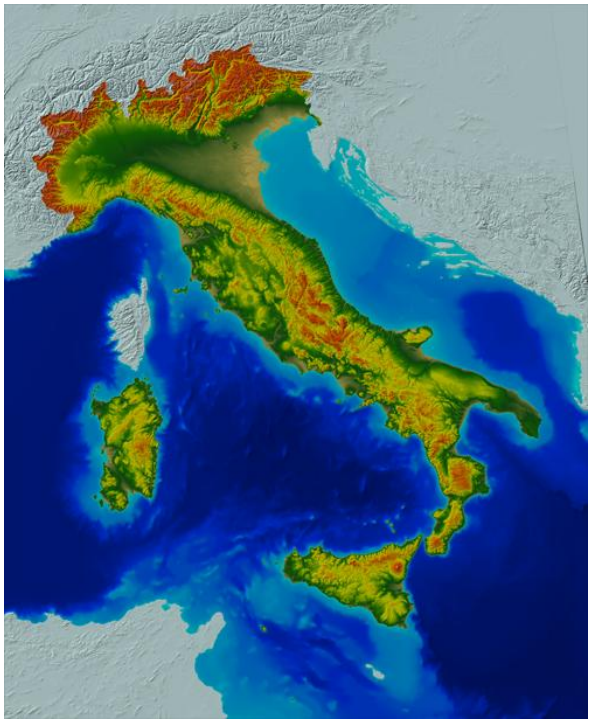

Figure 5 Overview of Tinitaly DEM over the Italian territory (source: https://tinitaly.pi.ingv.it/).

2.1.5 Groundwater withdrawals

We used groundwater withdrawals information collected between 2008 and 2024 as a proxy of anthropic pressure on aquifers. These data are gathered by Istat and distributed through IstatData platform in a systematic and harmonized way, keeping them updated and making information comparable across spatiotemporal scales. Specifically, annual groundwater withdrawals for potable use at regional scale in thousands of cubic meters have been retrieved (Figure 6). Then, pro-capita information at metropolitan city scale has been computed based on population data.

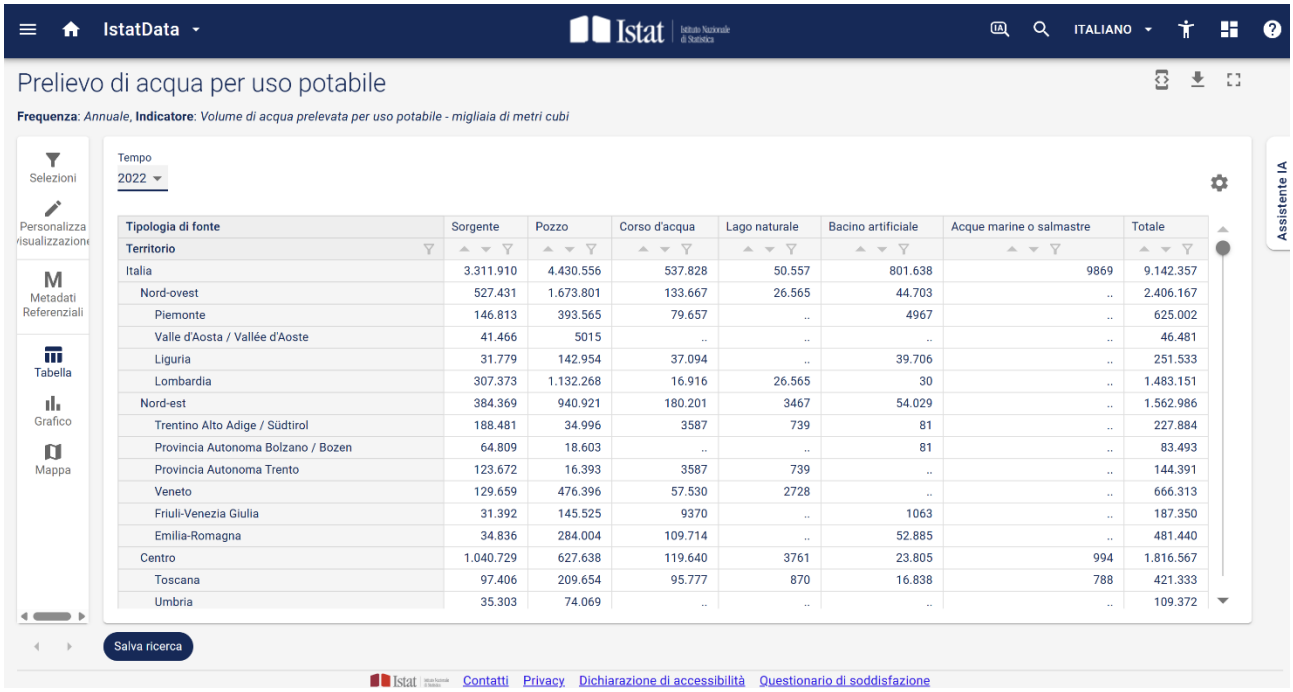

Tipologia di fonte / Territorio	Sorgente	Pozzo	Corso d'acqua	Lago naturale	Bacino artificiale	Acque marine o salmastre	Totale
Italia	3.311.910	4.430.556	537.828	50.557	801.638	9869	9.142.357
Nord-ovest	527.431	1.673.801	133.667	26.565	44.703	..	2.406.167
Piemonte	146.813	393.565	79.657	..	4967	..	625.002
Valle d'Aosta / Vallée d'Aoste	41.466	5015	..	..	..	..	46.481
Liguria	31.779	142.954	37.094	..	39.706	..	251.533
Lombardia	307.373	1.132.268	16.916	26.565	30	..	1.483.151
Nord-est	384.369	940.921	180.201	3467	54.029	..	1.562.986
Trentino Alto Adige / Südtirol	188.481	34.996	3587	739	81	..	227.884
Provincia Autonoma Bolzano / Bozen	64.809	18.603	..	..	81	..	83.493
Provincia Autonoma Trento	123.672	16.393	3587	739	..	..	144.391
Veneto	129.659	476.396	57.530	2728	..	..	666.313
Friuli-Venezia Giulia	31.392	145.525	9370	..	1063	..	187.350
Emilia-Romagna	34.836	284.004	109.714	..	52.885	..	481.440
Centro	1.040.729	627.638	119.640	3761	23.805	994	1.816.567
Toscana	97.406	209.654	95.777	870	16.838	788	421.333
Umbria	35.303	74.069	..	..	..	..	109.372

Figure 6 Overview of IstatData platform

2.2 Risk assessment methodology

The future risk mapping methodology over the 15 metropolitan cities is assessed building on the methodology developed at the national scale for present-day risk analysis in the SubRISK+ project (Cigna et al. 2025). A tailored methodology which ingests multi-temporal EGMS velocity rasters, along with bias-corrected climate predictors (precipitation, evapotranspiration), and an external time series of water withdrawal at metropolitan scale; calibrates a pixel-wise statistical model on the 2018–2022 period, and extrapolates annual subsidence rates to the target year. The model outputs are aggregated into cumulative vertical displacement, converted to angular distortion proxies on the exposure-vulnerability (EV) grid, classified into hazard (H) levels, and combined with EV to obtain risk maps. DEL6.2 illustrates the entire workflow for the assessment of risk components. Further details on each risk component are provided in the following sections.

2.2.1 Exposure-Vulnerability (EV)

As already described in recent works (DEL2.2; Cigna et al. 2025), the exposure–vulnerability (EV) assessment integrates information on the structure and evolution of the built environment to evaluate how urban areas may be affected by differential ground displacement. The approach combines spatial datasets describing building height (≤ 3 m, 3–6 m, 6–15 m, 15–30 m, > 30 m), type (residential or non-residential), and age (pre-/post-1985) with models of future urban expansion (Figure 7), allowing both present-day conditions and projected scenarios to be assessed at a consistent 100 m resolution.

The exposure–vulnerability assessment is developed through a sequential workflow (DEL6.2) that integrates spatial constraints, settlement data processing, temporal classification, and future urban-expansion modelling into a single coherent framework. The process begins by identifying where future development can realistically occur, that means by simulating the likely distribution of new built-up areas using a precautionary, regulation-based approach. It is to note that vulnerability assessments in this study do not depend on RCP scenarios since we did not focus on future projections based on emission pathways rather on possible urbanization and land cover changes dynamics.

A geospatial model identifies potential expansion zones by excluding areas unsuitable for development, based on: i) land cover (e.g., vegetation, protected areas), ii) DEM-derived factors (slope, elevation), iii) distance to infrastructure networks (roads, rail, buildings, utilities), iv) hydrological constraints. These constraints are essential to delineate the areas where urban growth is physically or environmentally feasible.

In parallel, all relevant settlement datasets are aligned to a common spatial resolution, ensuring that building height information from GHSL-S/C and construction age from WSF can be combined consistently after appropriate resampling and interpolation.

A temporal analysis is then performed to distinguish pre-1985 from post-1985 built areas, enabling the classification of the urban surface according to its construction period. Growth rates are calibrated using multi-date GHSL-S data, validating the simulation against the 2015 benchmark. A weighted mean across intervals yields a calibrated annual rate (bounded between 0 and 0.2), which is translated into a per-step transition probability (five-year steps). Using GHSL-S 2005 as the baseline, a cellular-automata model simulates urban growth to 2015 under neighbourhood/suitability weights ($\alpha = 0.3$, $\beta = 0.7$) and 100 stochastic realizations, producing an average urbanization probability surface. An optimal binarization threshold is selected by maximizing the F1 score against observed GHSL-S 2015 (with accuracy, precision, recall, F1 and Cohen's κ), yielding a validated 2015 baseline suitable for forward projection.

The forward simulation to the chosen target year proceeds with the same cellular-automata model settings but is constrained by a precautionary +3% cap over 2020-2050 on total urban area relative to 2015, that means that the total amount of new land consumption (i.e., conversion of non-urbanized land into urbanized land) cannot exceed 3% of the existing urbanized territory over this period. This limitation aims to significantly contain further soil sealing and urban sprawl over the reference period. Actually, there is no official national average since the regulatory frameworks are not standardized. This is a mean value in the range 2% – 5% of existing urbanized land over a 20–30 years planning horizon, which can be considered to represent a reasonable benchmark range for metropolitan contexts in Italy. This 3% threshold is further sustained by a Regional Law of Emilia Romagna region (Disciplina regionale sulla tutela e l'uso del territorio, L.R. 24/2017).

To enforce the cap, the code provides candidate pixels by simulated 2050 probability and activates only the top-ranked cells until the maximum allowed count is reached, ensuring spatial coherence while respecting policy constraints. This produces a 2050-2100 urban mask decomposed into persistent (2015) and newly urbanized (2016–2050/2100) pixels.

Where new growth is estimated, building heights are interpolated using an Inverse Distance Weighting (IDW) method applied to the heights of surrounding existing buildings. This follows the Italian national rule (Art. 6, Ministerial Decree 1444/1968), which requires new buildings to reference the prevailing height pattern of neighbouring structures. The result is a projected height raster for the near and far future, which is consistent with the local built form.

For the age dimension, the code aligns WSF Evolution to the GHSL-C grid and constructs a 2050/2100 age raster by assigning the value 2050 to pixels that urbanize after 2015; existing pixels retain their WSF-derived construction period (with a binary pre-/post-1985 interpretation as in the methods). These attributes are merged to produce a structural profile for each pixel, reflecting the assumption that taller buildings, non-residential structures, and older constructions are generally more vulnerable to ground deformation. Based on this logic, each pixel is assigned to one of four exposure–vulnerability classes, ranging from low (EV1) to very high (EV4). This results in a detailed spatial representation of current exposure and vulnerability across the metropolitan territory.

GHS-BUILT-C Settlement characteristics			WSF Evolution	
			≤ 1985	> 1985
Open spaces	01-05	low to high vegetation, water and road surfaces	n/a	
Built spaces, Residential	11	building height ≤ 3 m	EV2	EV1
	12	3 m < building height ≤ 6 m	EV3	EV2
	13	6 m < building height ≤ 15 m	EV3	EV2
	14	15 m < building height ≤ 30 m	EV4	EV3
	15	building height > 30 m	EV4	EV3
Built spaces, Non-residential	21	building height ≤ 3 m	EV2	EV2
	22	3 m < building height ≤ 6 m	EV3	EV2
	23	6 m < building height ≤ 15 m	EV3	EV3
	24	15 m < building height ≤ 30 m	EV4	EV3
	25	building height > 30 m	EV4	EV4

Figure 7 Example of Exposure-Vulnerability (EV) metric assessment approach

2.2.2 Hazard (H)

The hazard assessment forms the foundation of the WP6 approach, providing a consistent, data-driven method to quantify how land-subsidence processes evolve under changing climatic and anthropogenic conditions. To ensure reliability of future hazard projections, the modelling framework integrates multiple climate simulations and applies statistical correction techniques.

2.2.2.1 Data preprocessing

To ensure credible climate inputs, the hazard workflow incorporates an ensemble of GCM–RCM combinations (including CNRM-CM5, ICHEC-EC-EARTH, MPI-ESM-LR, HIRHAM5, RACMO22E, RCA4, and CCLM4-8-17, Table 1). This multi-model approach reduces structural uncertainty and yields a more robust representation of future conditions.

The raw RCM outputs exhibit systematic biases relative to observations. To ensure consistency across the entire 1970–2100 period, a bias-correction method based on the historical information for the adopted reference period (1970-2005) and the available RCM simulations has been used. These scenarios were derived for different emissions scenarios and the temporal horizon 2016-2045. Specifically, the bias-correction procedure applies a perturbation (transformation function) to the control series of the RCM simulations to obtain climate variables whose statistical properties more closely match those of the historical reference dataset. In the case of delta quantile mapping QDM (Teutschbein and Seibert 2012), the transformation function is derived by adjusting the modelled quantile distribution to reproduce the observed distribution, while preserving the climate-change signal. Unlike simple first- or second-moment correction methods, which focus on aligning only the mean and standard deviation, the QDM approach corrects the full distribution while retaining the modelled anomalies. The same transformation function, expressed in terms of delta changes rather than absolute values, is then applied to the future RCM simulations to generate bias-corrected climate projections that maintain the physically meaningful modelled shifts. An equifeasible ensemble of individual bias-corrected projections is subsequently constructed to produce a more robust and representative multi-model estimate of future climate conditions, reducing dependence on any single model outcome.

Following recent studies (Collados-Lara et al. 2018), simple regression models (linear and polynomial) have been tested to identify the best predictor combination for each metropolitan area reproducing vertical ground velocity as a function of different combinations of the predictors i.e., precipitation (pr), evapotranspiration (et) and groundwater withdrawals (ww). Evapotranspiration was calculated based on Blaney-Criddle method ($et=p(0.46t_{mean}+8)$), which is a function of the monthly mean temperature (t_{mean}) and latitude-derived sunshine hour fraction (p).

Annual potable water withdrawal in the 15 metropolitan cities (2008–2024) was obtained from ISTAT. Missing years were linearly interpolated, and the data were converted to per-capita withdrawal using the corresponding population records. Future water-use trajectories for 2023–2050 and 2023-2100 were generated under a baseline, trend-based scenario derived from linear regression.

2.2.2.2 Regression model calibration

To evaluate the relationship between subsidence and its climatic and anthropogenic drivers, a pixel-specific modelling framework was implemented. For each pixel climate predictors pr and et and ww were extracted and assembled into a local predictor matrix. Different model structures have been considered and tested to identify the best predictor combination for each metropolitan area. The resulting coefficients describe site-specific sensitivities of subsidence to climatic variables and water use.

Given the limited dataset consisting of only 5 yearly observations (2018 – 2022), we relied on a simple linear regression model mainly. This approach provides the most robust and statistically defensible option under severe data constraints, as it minimizes overfitting and ensures stable, interpretable coefficients. A ridge regression was also tested to stabilize coefficient to address multicollinearity, i.e., a regularization penalty to stabilize coefficient estimates when predictors are highly correlated is included. In the case of Napoli and Catania, where land deformation is dominated by volcanic and tectonic processes, which are largely independent of climatic forcing and groundwater withdrawal, simple trend extrapolation was tested as well. More complex or flexible models, such as polynomial regressions, were not considered appropriate, as they would consume too many degrees of freedom, produce unstable parameter estimates, and provide unreliable forecasts,

particularly outside the observed range. The linear approach therefore represents the best balance between model simplicity, interpretability, and predictive reliability given the available data.

Table 2 provides an overview of the regression models and variable transformations evaluated in the analysis. Model results for 2018–2022 were compared with observed EGMS velocities for validation and related skill was assessed using different evaluation metrics e.g., Root Mean Square Error (RMSE) and Pearson correlation coefficients.

Table 2 Tested regression models and variables

Model type	*pr, et*	*pr , ww*	*et, ww*	*et, ww, pr*	*trend-based*
Linear regression	*	*	*	*	–
Ridge-regularized linear regression	*	*	*	*	–
Trend-only extrapolation	–	–	–	–	*

2.2.2.3 Differential displacement and induced hazard

Future annual subsidence was simulated by driving the calibrated pixel-level models with RCP4.5 and 8.5 precipitation and evapotranspiration projections, combined with the selected groundwater withdrawal scenario. For each year between 2023 and 2100, climate variables and projected ww were inserted into the regression model to obtain future yearly displacement rates. Cumulative vertical displacements were then calculated by summing annual velocities over the selected horizon.

Accounting for the total vertical displacement over the 10-year historical period (2013–2022). near-future (2023–2050) and far-future (2023-2100), the associated hazard (H) levels for urban infrastructure are evaluated by computing the angular distortion (β), resulting from cumulative vertical displacements over each period. Specifically, the total vertical displacement d_U and the resulting angular distortion β are derived at each pixel as:

Total vertical displacement $\quad d_U = V_U \times t$

Total angular distortion $\quad \beta = \frac{d_{U_j} - d_{U_i}}{l}$

where $d_{U_j}$and d_{U_i}represent the vertical components at adjacent pixels $j$and i, l is their horizontal separation (taken as the 100 m spatial resolution of the EGMS Ortho grid), and t is the temporal length of the period considered (either 2013-2022, 2013-2050, or 2013-2100). To clarify the meaning of β, note that a distortion of 0.22% (1/450) in the 2013-2022 period corresponds to a differential vertical movement of 22 cm occurring over 10 years across a 100 m span.

Hazard levels are then assigned on a scale from low (H1) to very high (H4), representing an increasing likelihood of fissuring, fracturing, and associated damage to urban infrastructure. Thresholds for β follow established geotechnical criteria (Skempton and Macdonald 1956) and previous InSAR-based structural health studies (Cigna and Tapete 2021). For β, total angular distortion is categorized using thresholds of 1/3000 (0.033%), 1/1500 (0.067%), and 1/500 (0.200%); a 20% safety margin may optionally be applied to increase conservativeness.

The final hazard map is produced at 100 m resolution across each metropolitan area (Figure 8).

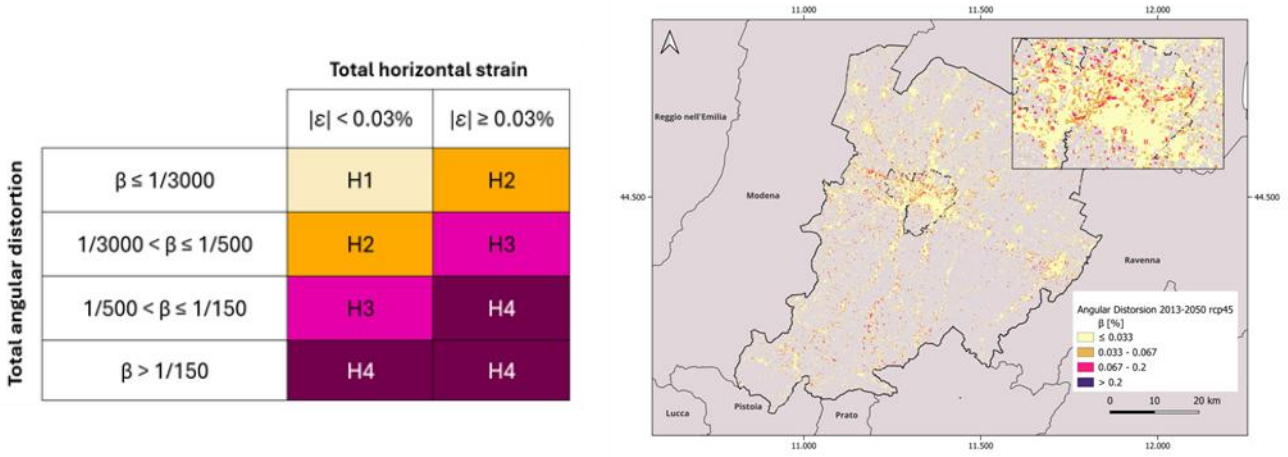

Figure 8 Example of Hazard (H) assessment and mapping using SubRISK+ methodology: total angular distortion and resulting H map.

2.2.3 Risk (R)

Finally, the H and EV layers are integrated through a tailored risk matrix, which enables the classification of risk into three levels.

- Low risk (R1) represents an acceptable condition that does not require specific intervention.
- Medium risk (R2) indicates that structural damage could plausibly occur in the affected urban areas; thus, dedicated monitoring of ground deformation and related stress indicators is recommended at the building-block scale.
- High risk (R3) corresponds to the most critical situation, pointing to a high likelihood of ongoing or incipient structural damage; in these cases, on-site inspections and targeted mitigation measures are advised at the individual-building scale.

An example of the resulting risk map is shown in Figure 9.

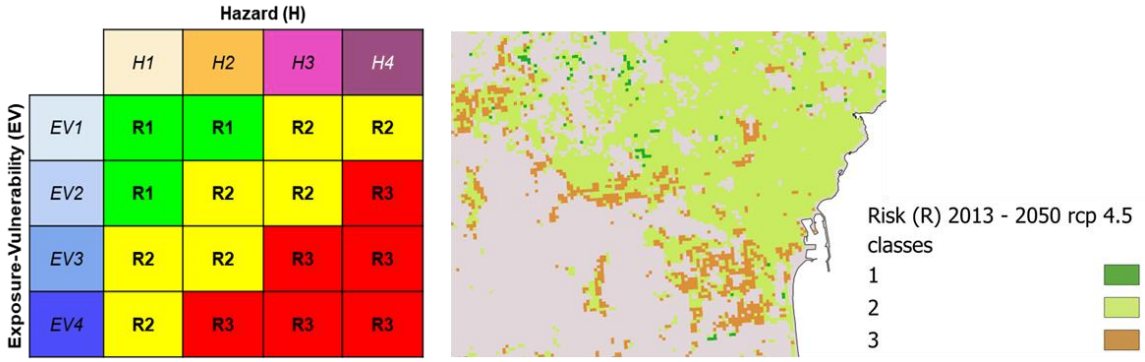

Figure 9 Example of Risk (R) assessment and mapping using SubRISK+ methodology: (a) risk matrix, and (b) resulting R map

3 RESULTS

3.1 Built-up expansion model calibration

This section showcases the main outputs of the calibration model to simulate built-up expansion in 2050 and 2100 in all 15 metropolitan cities in Italy.

Overall, the validation results indicate good agreement between the modelled expansion layer for 2015 and the GHSL-S2015 reference data across all metropolitan areas (Table 3). Accuracy values range from approximately 0.80 to 0.92, showing that the method correctly identifies the majority of built-up and non-built-up pixels. Cities such as Palermo, Catania, Messina, Napoli, and Cagliari achieve the highest accuracy (>0.88), reflecting a closer match between modelled expansion and GHSL.

Precision values display greater variability, from 0.597 (Sassari) to 0.927 (Napoli). High precision (e.g., Napoli, Milano, Genova) indicates a low false-positive rate, meaning that detected expansion corresponds well to actual built-up areas. Lower precision values, mainly in southern or island cities (e.g., Sassari, Palermo), suggest some overestimation of expansion.

Recall, ranging from 0.565 to 0.914, highlights differences in the model's ability to capture all existing expanded areas. Cities with high recall (e.g., Napoli, Catania, Genova) demonstrate strong completeness, while lower recall (e.g., Sassari, Venezia) points to missed expansion pixels.

F1 scores, which balance precision and recall, fall mostly between 0.70 and 0.85, confirming overall solid performance. The strongest F1 values appear in Napoli, Genova, Milano, and Catania, where both precision and recall are simultaneously high.

Cohen's κ values range from 0.51 to 0.74, indicating moderate to substantial agreement with GHSL-S2015 beyond chance. The highest κ values (Catania, Genova, Messina, Milano) reflect particularly robust classification, while lower values (Sassari, Firenze, Bologna) indicate areas where classification is more challenging, possibly due to mixed land-use patterns or more fragmented settlement structures.

The built-up expansion mapping approach performs consistently well across diverse urban contexts, with especially strong results in large metropolitan areas where urban growth is well defined and spatially coherent.

Table 3 Expansion validation 2015 vs GHSL-S2015 – Validation metrics

Metropolitan City	*Accuracy*	*Precision*	*Recall*	*F1*	*Cohen's κ*
Torino	0.847	0.804	0.751	0.776	0.660
Genova	0.864	0.879	0.830	0.854	0.726
Milano	0.836	0.861	0.811	0.835	0.671
Venezia	0.853	0.738	0.697	0.717	0.617
Bologna	0.825	0.752	0.691	0.720	0.593
Firenze	0.796	0.760	0.718	0.738	0.571
Roma	0.803	0.791	0.736	0.763	0.595
Napoli	0.876	0.927	0.914	0.920	0.648
Bari	0.844	0.725	0.691	0.708	0.601
Reggio Calabria	0.866	0.700	0.678	0.689	0.603
Palermo	0.912	0.697	0.654	0.675	0.624
Messina	0.898	0.766	0.727	0.746	0.683
Catania	0.919	0.808	0.767	0.787	0.737
Sassari	0.881	0.597	0.565	0.580	0.511
Cagliari	0.899	0.721	0.685	0.703	0.642

3.2 Application of correction techniques and propagation of climate and anthropic impact to subsidence

This section provides an overview of outputs of the correction techniques applied to RCM simulations under RCP4.5 and propagation of climatic and anthropic impact to subsidence through simple regression models. The initial model has been first calibrated on Bologna metropolitan city and then exported to the other metropolitan cities. Thus, in this section, outputs for this case study are presented as a representative example of the bias-correction procedure, since the qualitative performance of QDM is consistent across all metropolitan cities, and additional plots would therefore be redundant. Nevertheless, a summary of the model selection for each metropolitan city is also available at the end of the section.

All statistics presented in Figures 10 to 15 refer to monthly total precipitation and mean temperatures for the historical period 1970–2005. The distributional characteristics visible in the plots therefore reflect the month-to-month variability of the regional climate and provide an appropriate basis for evaluating the performance of the bias-correction procedure at the temporal scale required for the subsidence model.

Figure 10 compares the monthly precipitation climatology derived from observations (EOBS), raw CORDEX model output, and bias-corrected (QDM) simulations over the historical period, including the ensemble mean and the associated model uncertainty. The observed seasonal cycle (black line) shows the characteristic pattern of the region, with peak precipitation in autumn (months 10–11), a secondary maximum in late winter (month 2), and a pronounced summer dry minimum (months 6–7). The raw ensemble mean (blue dashed line) reproduces the general shape of the seasonal cycle but systematically overestimates precipitation in most months, particularly in winter and autumn. The raw model uncertainty envelope (light blue shading, ±1σ) is wide, indicating substantial spread

among individual models and highlighting inconsistencies in representing both winter peaks and the dry summer minimum.

After bias correction, the ensemble mean (orange line) aligns more closely with observed values throughout the year. The QDM-corrected uncertainty band (light orange shading) is consistently narrower than that of the raw ensemble, suggesting that bias correction effectively reduces inter-model dispersion. The improvement is particularly visible in spring and early autumn, where the bias-corrected mean closely follows observations. Nonetheless, some small deviations persist, for example a slight underestimation in late autumn and a residual wet bias in winter. Overall, the plot demonstrates that QDM substantially improves both the central tendency and the spread of the model ensemble, providing a seasonal cycle more consistent with observations while still retaining model uncertainty.

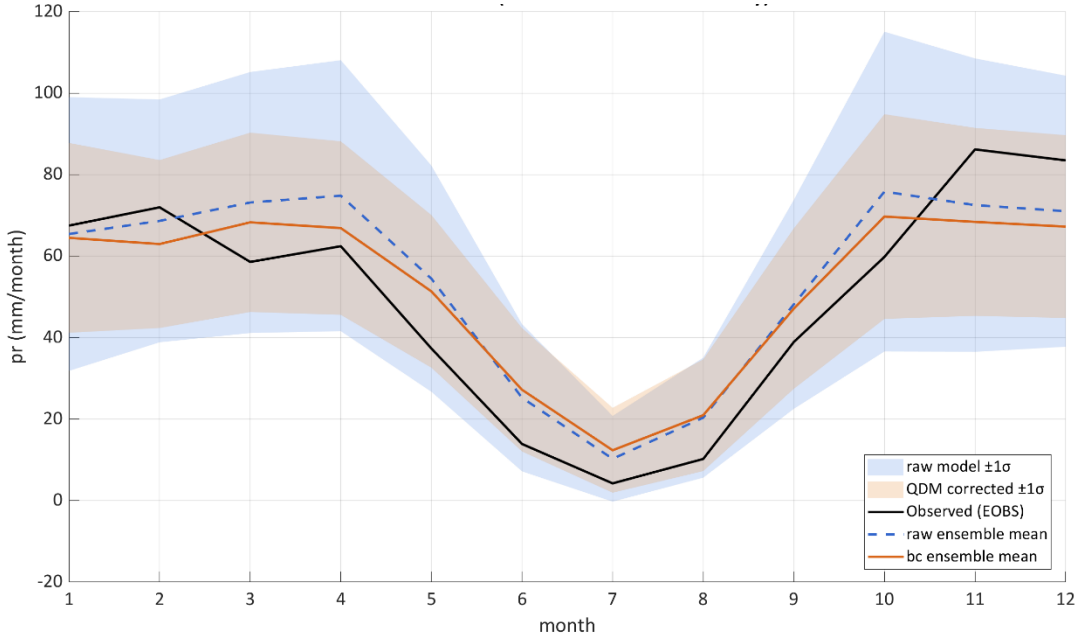

Figure 10 Monthly mean for the historical and RCM series (precipitation) for the mean year in the period 1970-2005 in Bologna metropolitan city

As can be seen in Figure 11, the raw CORDEX data exhibit a systematic wet bias, with a noticeably higher median monthly precipitation and a broader interquartile range compared to the observations, as well as an overestimation of the upper tail of the distribution. After applying quantile mapping, the central portion of the distribution aligns much more closely with EOBS, indicating an effective correction of biases in typical monthly conditions. However, the highest quantiles remain overestimated, and the corrected dataset still shows a tendency to produce excessively wet months relative to the observations. This behaviour is also evident in the QQ-plots, where the bias-corrected series follows the 1:1 line for low and intermediate quantiles but diverges for the most extreme precipitation months (Figure 12). Overall, the QM method substantially improves the representation of monthly precipitation but does not fully correct the bias in extreme events.

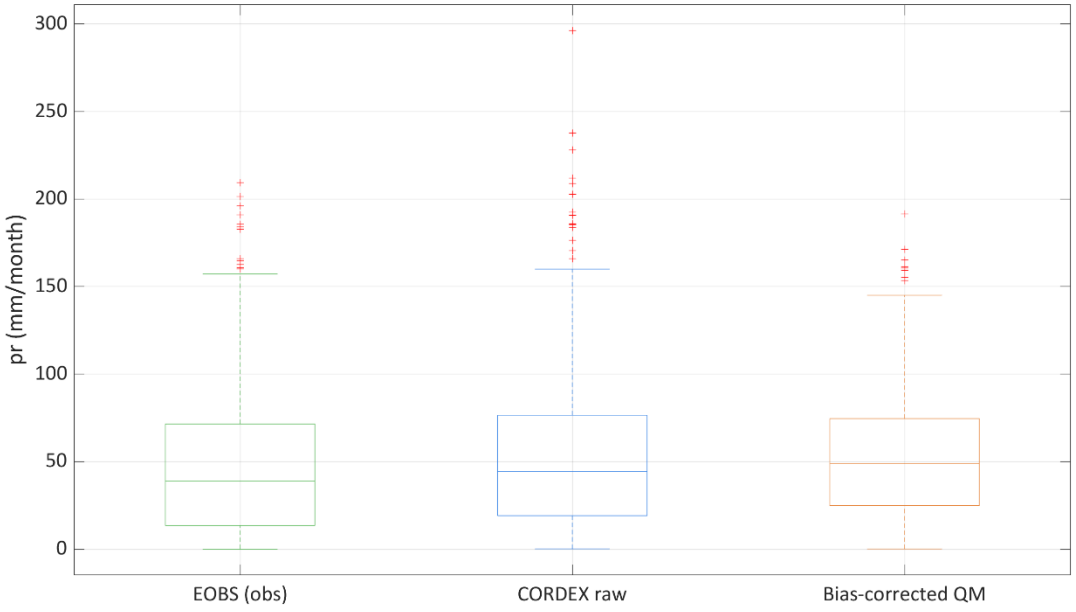

Figure 11 EOBS, CORDEX raw data and bias-corrected QDM distributions of mean monthly precipitation in Bologna metropolitan city

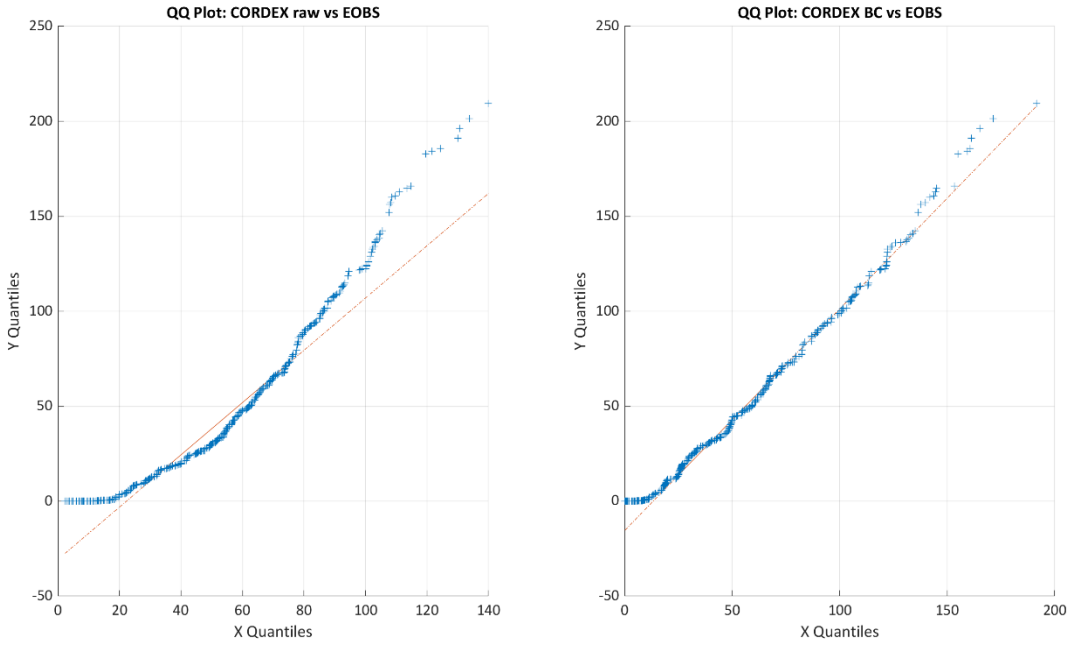

Figure 12 QQ plot showcasing CORDEX raw precipitation data before and after bias correction based on E-OBS in Bologna metropolitan city

Figure 13 compares monthly temperature climatology of the raw CORDEX ensemble, the QDM-corrected ensemble, and the EOBS observations over the historical period. The raw ensemble mean (blue dashed line) displays a marked cold bias from January to May up to approx. 1.5 °C below observations, and a moderate warm bias during July-August, with a broad uncertainty band reflecting substantial inter-model spread. After bias correction, the QDM ensemble mean (orange line) aligns much more closely with the EOBS seasonal cycle (black line) across all months. The winter–spring cold bias is largely eliminated, and the summer peak is corrected toward observations, although a slight residual warm bias persists. The QDM uncertainty band is also narrower than the raw ensemble, indicating reduced inter-model divergence following correction. Overall, the climatology illustrates that QDM effectively improves both the magnitude and the seasonal evolution of modelled temperatures, producing a much more realistic annual cycle.

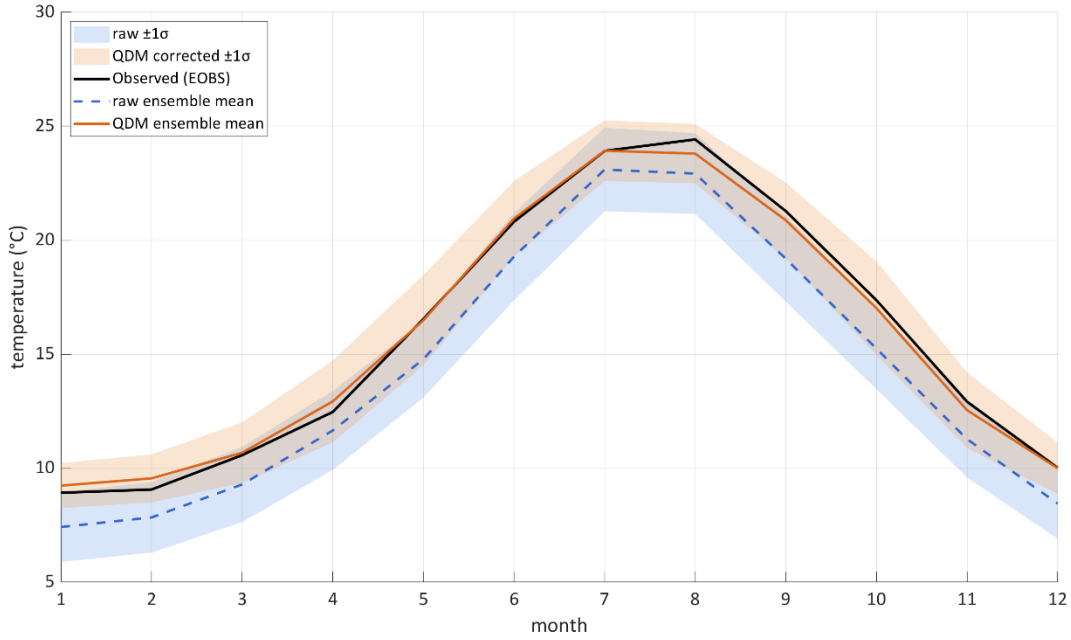

Figure 13 Monthly mean for the historical and RCM series (temperature) for the mean year in the period 1970-2005 in Bologna metropolitan city

Figure 14 shows that the raw ensemble underestimates observed temperatures across most of the distribution, whereas the QDM-corrected series aligns closely with EOBS, particularly in median and interquartile range. QQ-plots (Figure 15) confirm that QDM improves the entire distribution, bringing model quantiles much closer to the 1:1 line except for minor deviations at the highest quantiles. The monthly climatology further highlights these improvements: the raw ensemble is systematically too cold in winter and spring and slightly too warm in summer, while the QDM-corrected cycle closely reproduces the observed seasonal pattern with reduced spread.

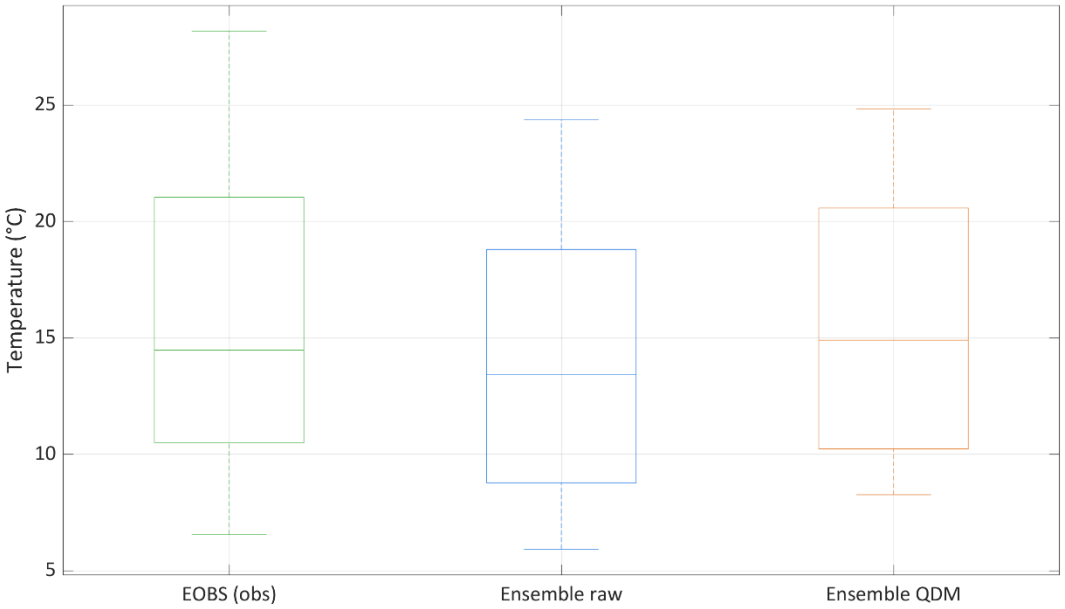

Figure 14 EOBS, CORDEX raw data and bias-corrected QDM distributions of mean monthly temperature in Bologna metropolitan city

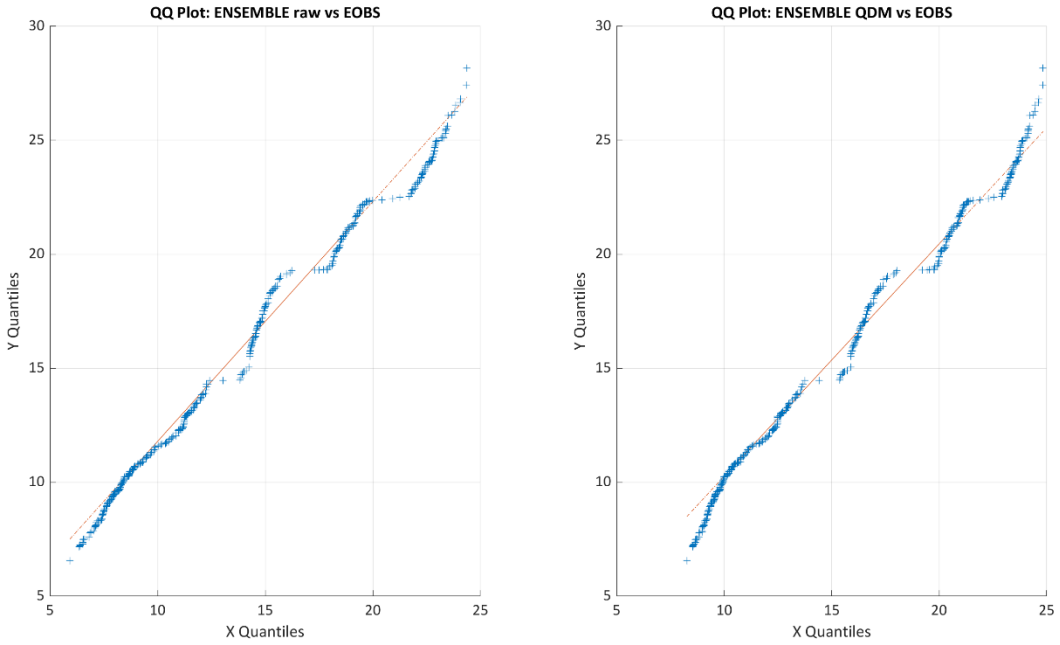

Figure 15 QQ plot showcasing CORDEX raw temperature data before and after bias correction based on E-OBS in Bologna metropolitan city

Bias-correction improves the consistency of both precipitation and temperature simulations with observations (Table 4). For precipitation, QDM reduces the monthly RMSE and the wet bias, indicating a moderate but meaningful improvement in the representation of rainfall totals. For temperature, the effect is markedly stronger: the raw ensemble exhibits a clear cold and an RMSE of 2.01 °C, while QDM nearly eliminates the bias (–0.02 °C) and reduces the RMSE to 1.31 °C.

Table 4 Performance of bias-correction on mean monthly precipitation and temperatures in Bologna metropolitan city

Error metric	pr	tas
RMSE (RAW vs EOBS)	40.25 mm/month	2.01 °C
RMSE (QDM vs EOBS)	38.94 mm/month	1.31 °C
BIAS (RAW vs EOBS)	5.45 mm/month	-1.49 °C
BIAS (QDM vs EOBS)	2.90 mm/month	-0.02°C

Although QDM significantly improves the alignment between observed and simulated monthly precipitation distributions, some residual bias remains in the upper tail. This behaviour is expected and can be attributed to several factors. First, regional climate models typically exhibit a systematic over-representation of very wet months, a structural bias that cannot be fully removed when monthly accumulation integrates diverse processes such as convective storms and large-scale frontal systems. Second, QDM preserves the relative climate-change signal, which limits the extent to which extremely high quantiles can be adjusted without distorting the projected anomalies. Finally, the limited number of extreme months in the historical record reduces the robustness of percentile-based corrections in the upper tail. As a result, while the central part of the distribution is effectively corrected, the most intense precipitation months remain more uncertain and retain some degree of overestimation.

The bias-corrected future time series shows that, under the RCP 4.5 scenario, mean annual precipitation in the Bologna metropolitan area is projected to decline by approximately 9.7 % and 10.8 % over 2021–2050 and 2100 relative to the 1991–2021 baseline (Figure 16). This reduction aligns with broader regional projections for the northern Apennines and the wider Mediterranean basin, where a gradual decrease in total rainfall and an intensification of seasonal variability is expected (Arpae Emilia-Romagna 2026). Such changes are often associated with longer dry spells, more concentrated rainfall events, and increased hydroclimatic stress during summer months.

Mean annual temperature for 2021–2050 and 2100 is estimated to increase by approximately 8.4% and 14.1 %, reflecting the robust warming pattern reported across most climate models for southern Europe. This rise is particularly relevant for hydrological processes: higher temperatures can enhance potential and actual evapotranspiration, accelerate soil-moisture depletion, and increase water demand in both natural and anthropic systems. The combined effect of slightly reduced precipitation and substantially higher temperatures therefore points to a future climate characterised by greater atmospheric evaporative demand and potentially more frequent water-stress conditions.

Figure 17 illustrates these tendencies by comparing historical and projected bias-corrected 30-year windows for precipitation and temperature. The figure highlights the persistence of the warming trend and the subtle but consistent decline in rainfall, both of which are key inputs to the subsidence modelling framework.

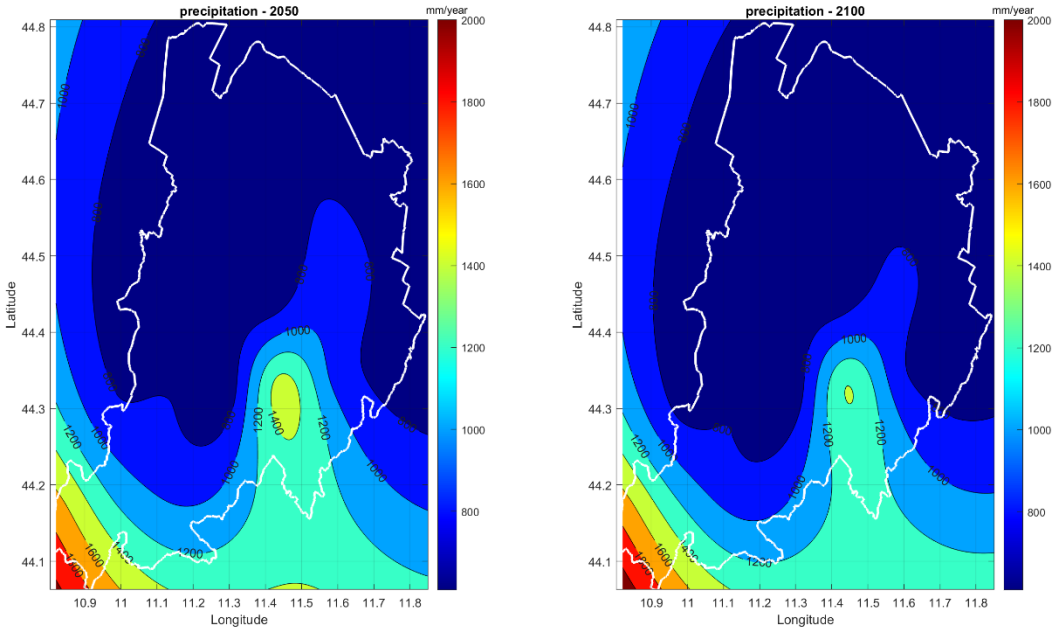

Figure 16 Example of spatially interpolated precipitation values in 2050 and 2100 under rcp4.5 in Bologna metropolitan city

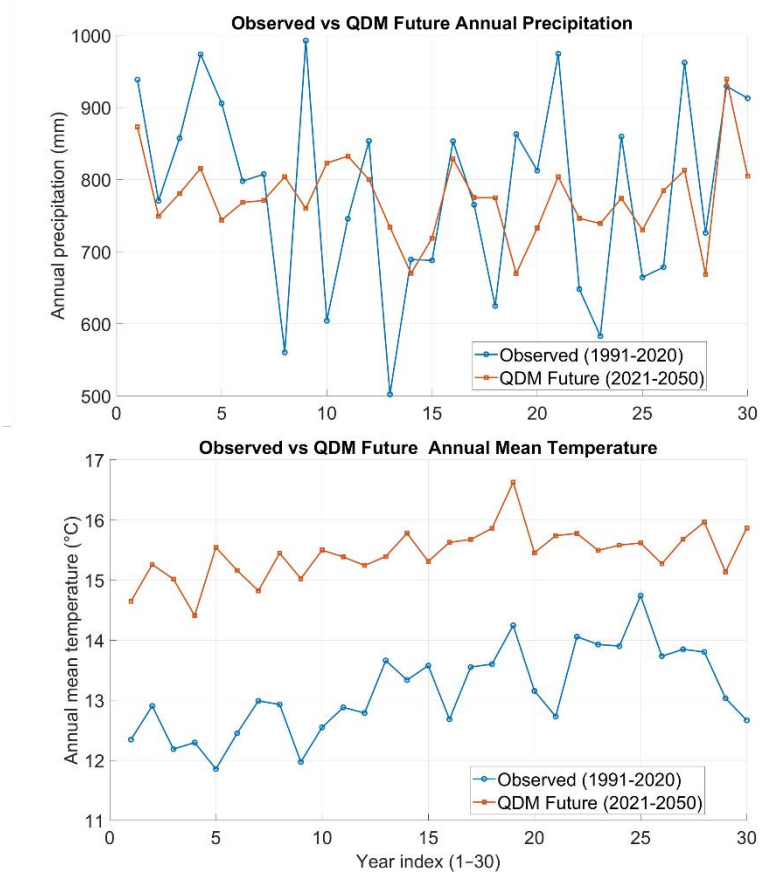

Figure 17 Yearly average observed and projected bias-corrected time series of total precipitation and mean temperature for 30-year windows 1991–2020 and 2021–2050 in Bologna metropolitan city under RCP 4.5.

Taking into account projected changes in future local climate series and groundwater withdrawal, different linear regression models have been used to assess future vertical ground displacements. The best performing model for Bologna metropolitan city turned out to be a ridge regression linear model based on the combination of pr and ww, showing, across all considered years, an average rmse = 2.572 mm, mse=6.747 mm^2, average Pearson = 0.90, rmse=0.812 and r/rmse=0.322.

An overview of the selected models across all metropolitan cities is provided in Table 6. Model performance varied substantially among the metropolitan areas, reflecting the differing deformation mechanisms that characterize each region. In most cities, precipitation and evapotranspiration emerged as the most informative predictors, although with modest explanatory power (r/rmse typically between 0.10 and 0.28), indicating a generally weak but detectable climatic control on annual subsidence rates. Bologna represents an exception: here, the inclusion of water-withdrawal data markedly improved the model fit (r/rmse = 0.32), consistent with the known sensitivity of the local aquifer system to extraction. Firenze also displayed relatively high performance (r/rmse = 0.39), suggesting a stronger correlation between ground motion and hydro-climatic variability. In Napoli and Catania, land deformation is dominated by volcanic and tectonic processes, which are largely independent of climatic forcing and groundwater withdrawal. For these cities, climate variables may not explain their temporal variability for these cities, thus a simple trend-based extrapolation of observed displacement was used as considered more appropriate than a climate-driven statistical model. Finally, several southern cities (e.g., Bari, Messina, Cagliari) showed very low r/rmse values (~0.10), indicating either low-amplitude displacement,or processes largely decoupled from climatic drivers.

Table 6 Selected model and related r/rmse metric for each metropolitan city

Metropolitan city	*Model*	*r/rmse*
Torino	pr, et	0.19
Milano	ww, et	0.21
Genova	pr, et	0.14
Venezia	pr, et	0.22
Bologna	pr, ww	0.32
Firenze	pr, et	0.39
Roma	pr, et	0.28
Napoli	trend-based	0.39
Bari	pr, et	0.1
Reggio Calabria	pr, et	0.19
Messina	pr, et	0.1
Palermo	pr, et	0.23
Catania	trend-based	0.1
Sassari	pr, et	0.13
Cagliari	pr, et	0.1

3.3 Overview of differential displacements risk in Italy

Figures 18 to 21 illustrate the projected distribution of land-subsidence hazard classes (H1–H4) across Italian metropolitan cities for the mid-century (2050) and end-century (2100) periods under the RCP 4.5 and 8.5 climate scenarios. The classification is based on trend-based vertical ground-displacement estimates incorporating climate-driven changes in precipitation and evapotranspiration, as well as groundwater-withdrawal patterns. As can be seen, there are no significant visual differences between the two RCPs in 2050s, since in both scenarios, the hazard distribution across Italian cities follows a very similar pattern. The lack of divergence between RCP 4.5 and RCP 8.5 at the 2050 milestone suggests that, according to these models, the hazard levels for the next few decades are already largely determined, with the major differences between the emission scenarios only becoming clearly visible toward the end of the century (as seen in the 2100 projections). By the end of the century, both scenarios project a sharp increase in hazard levels compared to 2050.

Even at the 2100 mark, the visual and statistical distribution of H1 through H4 is nearly mirrored between the two scenarios, suggesting that the hazard peaks reached in these models are consistent across both climate paths for these specific urban areas. Cities such as Bologna, Firenze, and Bari consistently show the most aggressive shift toward higher hazard classes (H3 and H4) by 2100 in both RCP scenarios. The area covered by the lowest hazard level (H1) drops significantly in both scenarios, falling to 30-60% for most cities. The high hazard class (H3) expands drastically. In cities like Bari, Bologna, Firenze, and Reggio Calabria, H3 grows to cover roughly 25% to 40% of the urban territory in both RCP 4.5 and RCP 8.5. The maximum hazard level (H4) appears in nearly all cities, though it remains a small percentage of total coverage (estimated at 2-5%) in both scenarios. Thus, these results indicate a marked upward shift in hazard severity over time rather than over different scenarios.

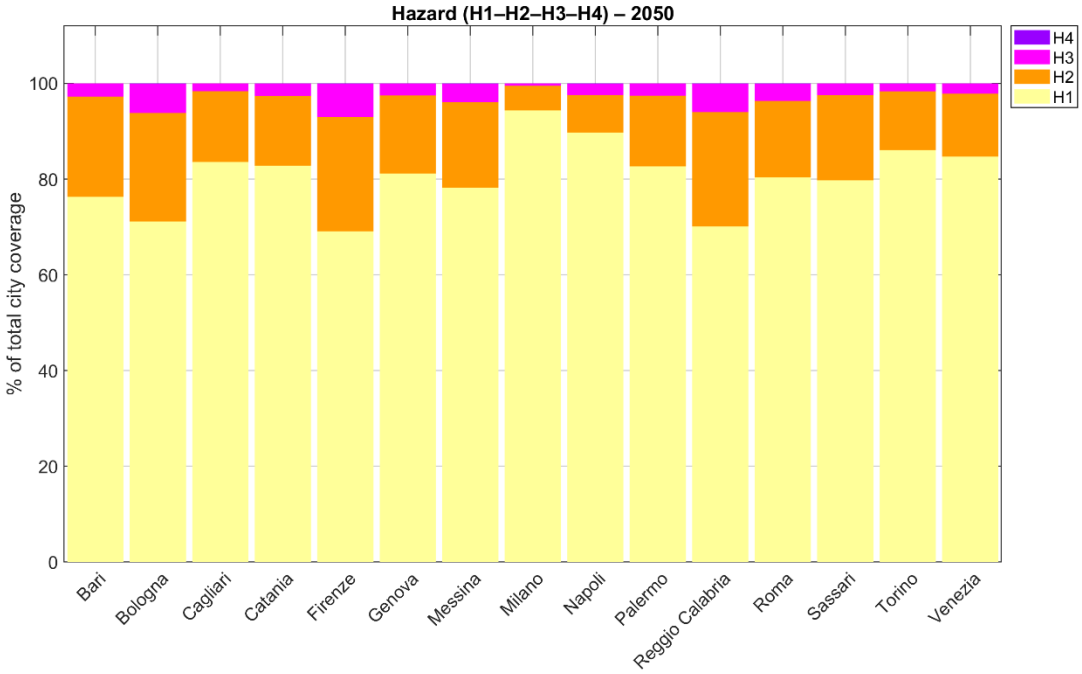

Figure 18 Extent of the four Hazard (H) classes within each metropolitan city in 2050 under rcp4.5, displayed using a percentage scale (100% refers to the total extent of the hazard data within each city), and derived by following the method described in section 2.2.2

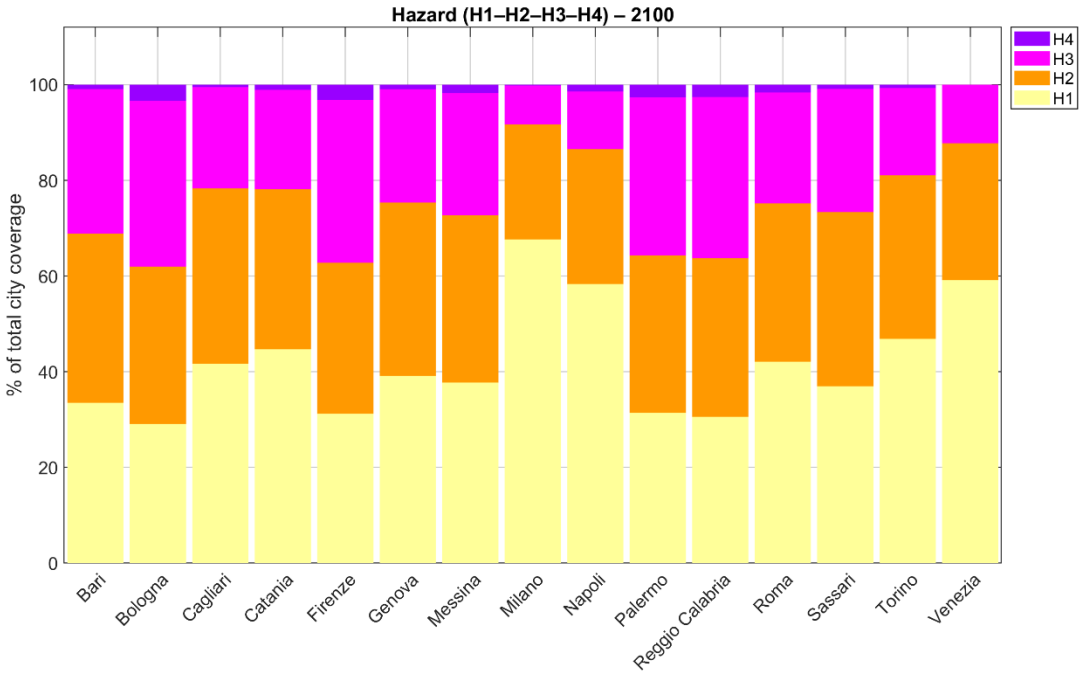

Figure 19 Extent of the four Hazard (H) classes within each metropolitan city in 2100 under rcp4.5, displayed using a percentage scale (100% refers to the total extent of the hazard data within each city), and derived by following the method described in section 2.2.2

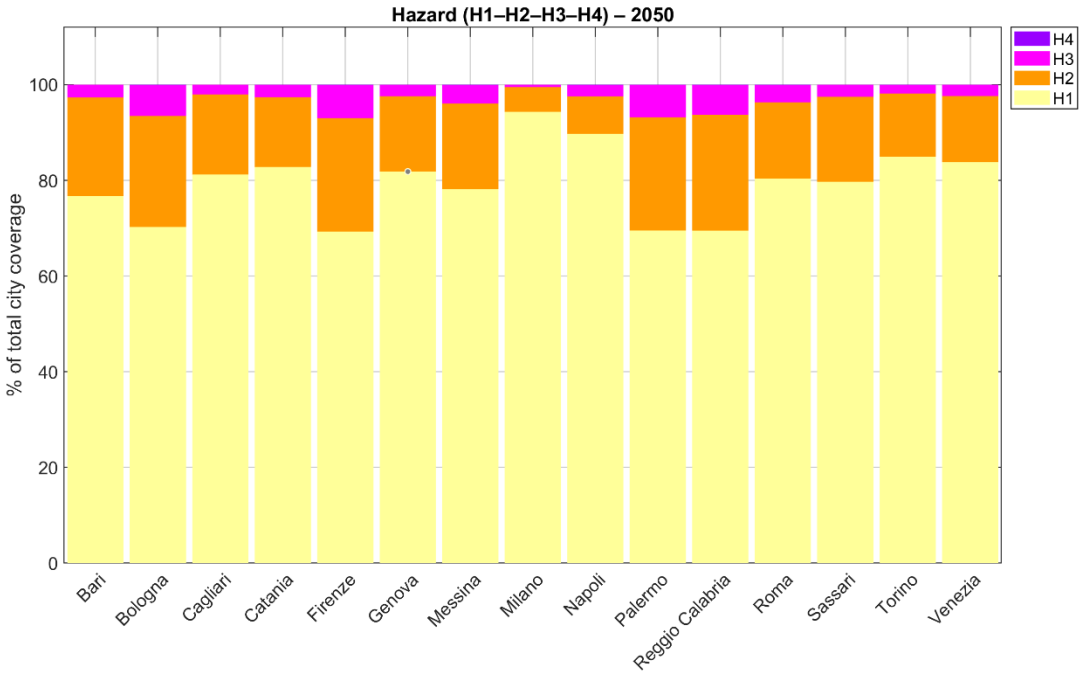

Figure 20 Extent of the four Hazard (H) classes within each metropolitan city in 2050 under rcp8.5, displayed using a percentage scale (100% refers to the total extent of the hazard data within each city), and derived by following the method described in section 2.2.2

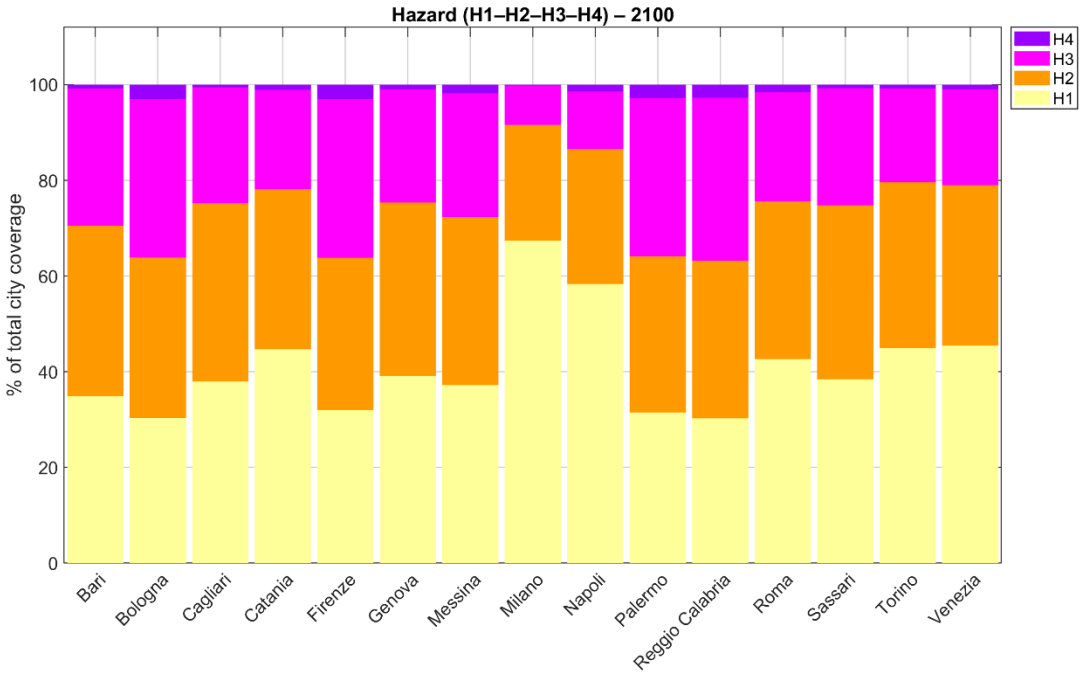

Figure 21 Extent of the four Hazard (H) classes within each metropolitan city in 2100 under rcp8.5, displayed using a percentage scale (100% refers to the total extent of the hazard data within each city), and derived by following the method described in section 2.2.2

The spatial distribution of Exposure–Vulnerability classes (EV1–EV4) across the metropolitan areas under study is shown in Figures 22-23. These classes integrate multiple dimensions of urban sensitivity to differential ground displacement, including building height, construction age, structural density, and the spatial configuration of current and future urban development.

The classification reveals that no areas fall within the Low Exposure–Vulnerability (EV1) class. The Medium Exposure–Vulnerability (EV2) class occupies 5–19.5% of urban land, with the highest proportions found in Sassari, Messina, and Bologna (approximately 15.5–19.5%).

Most of the metropolitan land is classified as High Exposure–Vulnerability (EV3), accounting for over 65% of mapped areas. This class reaches its highest values, around 82–84%, in Rome, Reggio Calabria, Naples, and Palermo, reflecting their dense and structurally complex urban fabrics.

The Very High Exposure–Vulnerability (EV4) class ranges from 3% to 28%, with the largest extents observed in Milan (~28%), Bologna (~17%), and Genoa (~15.5%). These cities exhibit concentrated clusters of vulnerable infrastructure combined with limited opportunities for low-risk urban expansion.

These results underscore the structural susceptibility of Italian metropolitan areas to future ground-displacement impacts, driven by dense settlement patterns, aging buildings, and high infrastructural exposure.

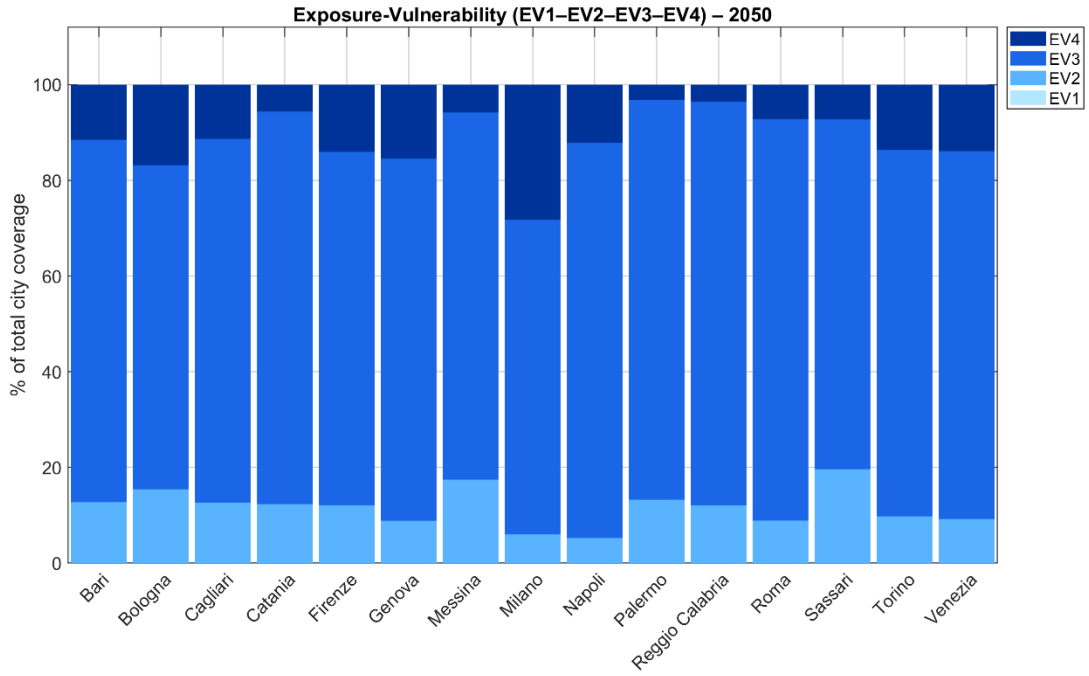

Figure 22 Extent of the four Exposure-Vulnerability (EV) levels within each city in 2050, derived by following the method described in section 2.2.1

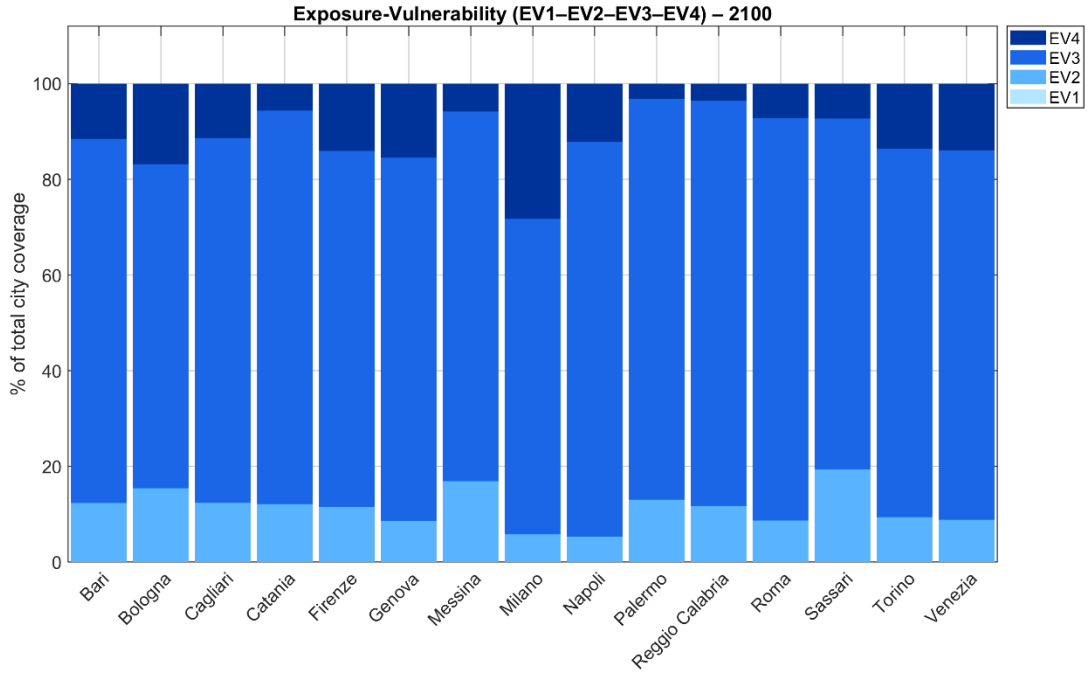

Figure 23 Extent of the four Exposure-Vulnerability (EV) levels within each city in 2100, derived by following the method described in section 2.2.1

The resulting classification identifies three risk levels (R1–R3) projected for 2050 and 2100 under the RCP 4.5 and 8.5 emissions scenarios (Figure 24 to Figure 27). This assessment provides an integrated understanding of the potential impacts of land subsidence on metropolitan areas by considering not only the physical likelihood of ground displacement, but also the degree to which urban assets are exposed and structurally vulnerable.

Across all metropolitan cities, the risk distribution is characterized by a predominance of Medium Risk (R2) areas, accompanied by smaller fractions of Low Risk (R1) and expanding zones of High Risk (R3). The observed shifts between 2050 and 2100 reflect both the intensification of land-subsidence hazard and persistent high levels of urban exposure and vulnerability.

The Low Risk (R1) class represents only a marginal portion of the mapped urban land. In 2050, 1–4% of the analysed territory falls into this category, indicating limited overlap between low hazard levels and moderate-to-low exposure. By 2100, this proportion declines further to 0.5–2%, reflecting the general upward trend in hazard severity and the structural permanence of high exposure in dense metropolitan contexts. These small fractions underscore that very few urban zones retain conditions capable of dampening the combined hazard–vulnerability effect.

By the end of the century, R2 risk area generally reduces as they are replaced by R3. However, the extent of this contraction varies by city and emission scenario. Milano maintains the highest percentage of R2 risk, still covering approximately 90% of the city. This is because, despite high vulnerability, the climate-related hazard level remains relatively moderate compared to other cities. Napoli and Torino also retain high R2 levels, around 85-90% coverage. In general, by 2100, the prevalence remains high, with values between 76% and 90%. This persistence indicates that most cities are projected to experience moderate–high interactions between subsidence hazard and the structural vulnerability of the urban fabric. The broad extent of R2 areas suggests that many urban districts are likely to be affected by meaningful but not yet critical subsidence impacts. This includes zones with increasing hazard levels but without the extreme exposure–vulnerability combinations that would push them into R3. R2 therefore represents a substantial challenge for urban planning, as it encompasses areas where impacts may be widespread and cumulative, requiring systematic mitigation strategies.

By 2100, the distribution of the maximum risk level R3 across shows a generalized and marked increase compared to the mid-century, with significant differences between the two emission scenarios for certain locations. Bologna is the most critical city. In the RCP 4.5 scenario, the R3 class covers approximately 40% of the territory. However, in the RCP 8.5 scenario, this percentage dramatically surges, reaching about 70% of the city's surface. Firenze shows a high and consistent level of risk in both scenarios, with the R3 class accounting for around 35% of the total coverage. Palermo and Reggio Calabria see the R3 class extending over a significant portion of their territory, roughly between 20% and 25%. A large group of cities, including Bari, Cagliari, Catania, Genova, Messina, Roma, Sassari, and Venezia, presents a similar R3 risk distribution, generally oscillating between 15% and 20% of the urban area in both climate scenarios.

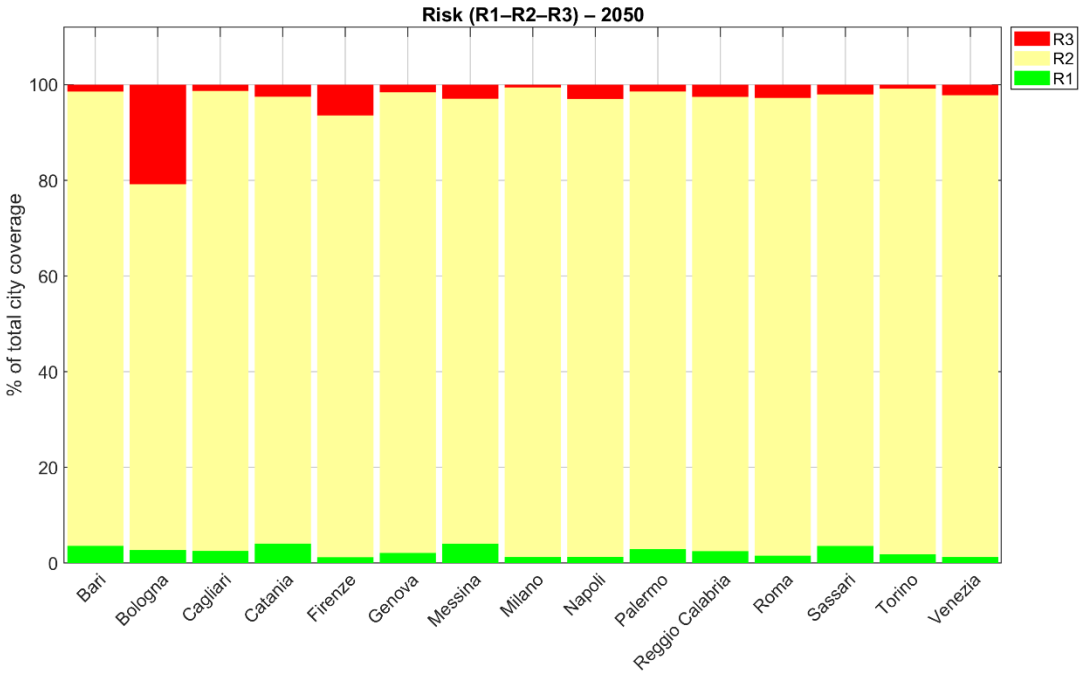

Figure 24 Extent of the three Risk (R) classes within each of the 15 metropolitan cities of Italy in 2050 under rcp4.5, derived by following the method described in section 2.2.3.

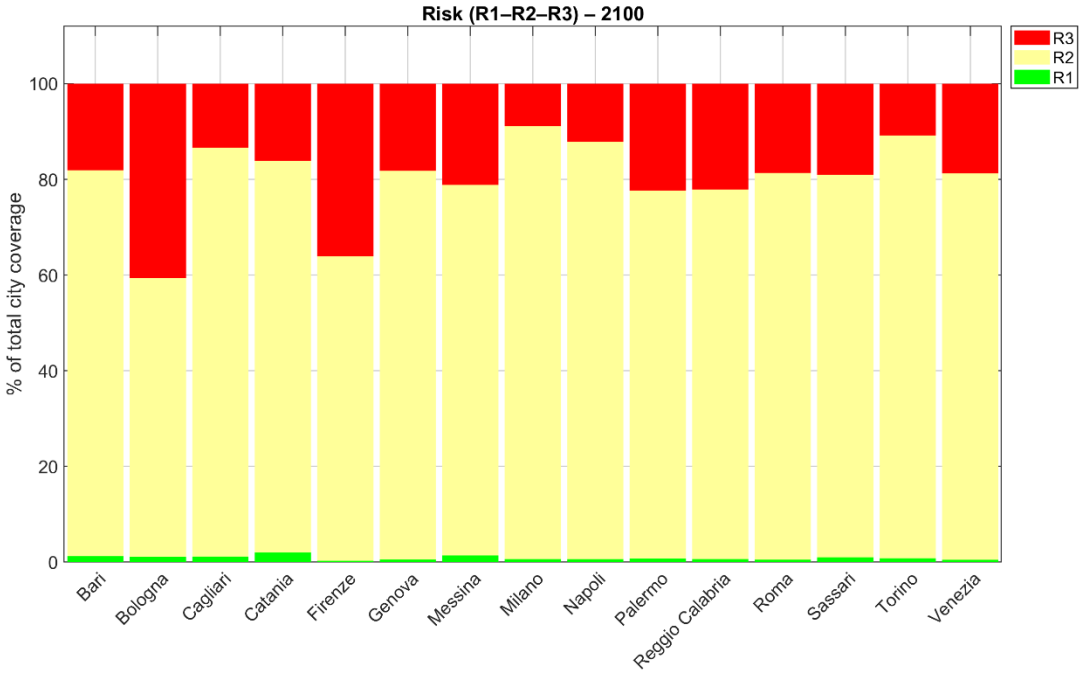

Figure 25 Extent of the three Risk (R) classes within each of the 15 metropolitan cities of Italy in 2100 under rcp4.5, derived by following the method described in section 2.2.3.

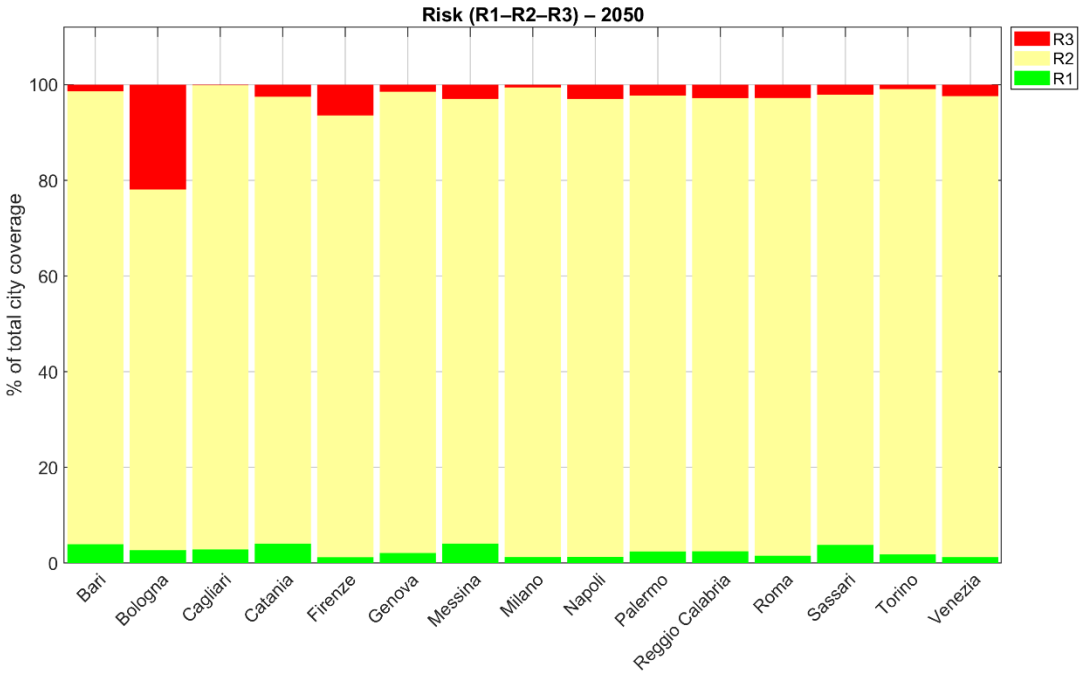

Figure 26 Extent of the three Risk (R) classes within each of the 15 metropolitan cities of Italy in 2050 under rcp8.5, derived by following the method described in section 2.2.3.

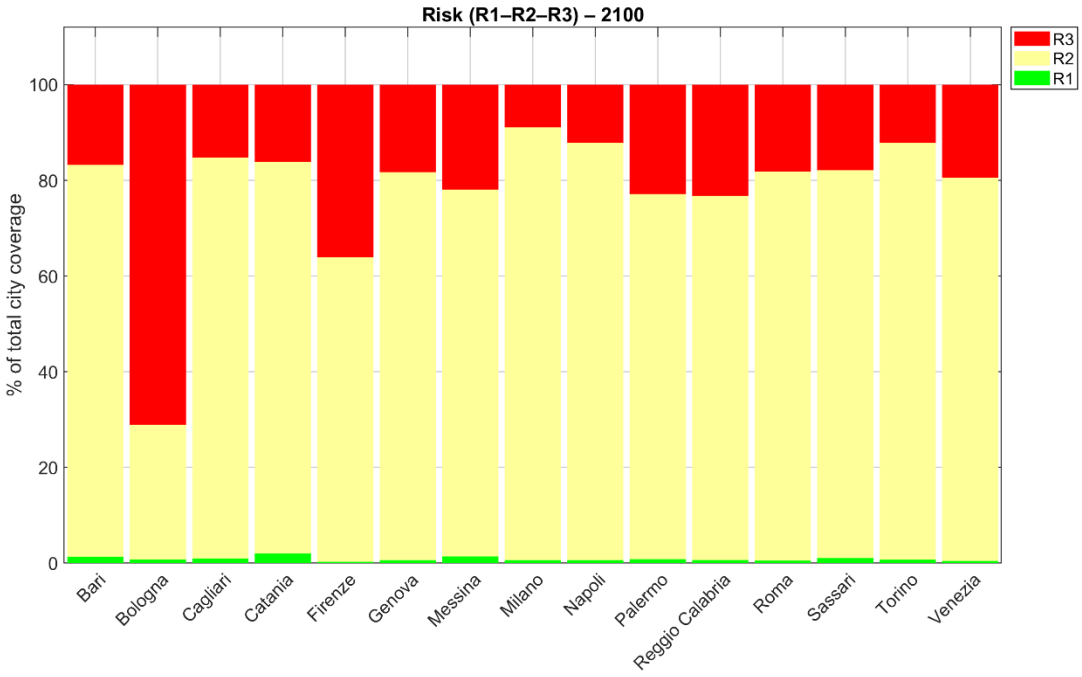

Figure 27 Extent of the three Risk (R) classes within each of the 15 metropolitan cities of Italy in 2100 under rcp8.5, derived by following the method described in section 2.2.3.

3.4 City-specific risk mapping

The full set of maps (exposure-vulnerability, hazard and risk) generated for each of the 15 metropolitan cities of Italy is available in DEL6.1

The hazard, exposure–vulnerability and resulting risk maps can be interactively explored through the SubRISK+ *Control Room* platform (https://controlroom.subrisk.eu), where digital versions of all layers are available for open visualization and navigation.

4 CONCLUSIONS

The analysis presented in this study offers an integrated assessment of future land-subsidence dynamics across Italian metropolitan areas, drawing on ground-deformation observations, climate-driven hazard projections, and a detailed characterization of urban exposure and vulnerability. The results indicate that subsidence-related impacts are expected to intensify throughout the twenty-first century, not only under the worst-case scenario but even under moderate emission pathways and conservative assumptions on future urban expansion.

While the methodology provides a scalable and coherent framework for national-level subsidence risk assessment, several limitations must be considered when interpreting the projections. First, the regression models are calibrated using only five years of EGMS observations (2018–2022). Although these data are consistent and high quality, they may not capture longer-term deformation cycles such as slow compaction, variable groundwater management, or intermittent uplift. Second, the empirical relationships between subsidence and climatic or anthropogenic predictors are assumed to remain constant through 2050 and 2100, whereas real-world hydrological and human-driven processes may evolve non-linearly. The projections should therefore be regarded as scenario-based rather than deterministic. Additionally, groundwater-withdrawal trajectories are estimated using a trend-based continuation of past patterns, without accounting for possible policy changes, infrastructure improvements, or shifts in water-use behaviour. As a result, forecasts for cities historically affected by aquifer depletion (e.g., Bologna, Milano) need caution. The statistical nature of the modelling also means that physical hydro-mechanical processes are not explicitly simulated. Hazard is derived at the 100 m resolution of EGMS Ortho products and relies on angular-distortion thresholds originally developed at building scale, which may smooth localised deformation hotspots. The exposure–vulnerability component, based on a precautionary assumption of up to 3% additional urbanisation between 2022 and 2050, further reflects uncertainties related to future planning choices, construction practices, and adaptive measures.

Results suggest that the increase in risk and hazard levels is more relevant across decades rather than emission scenarios. Differences between RCP4.5 and RCP8.5 climate projections are expected to remain small until mid-century, particularly for precipitation and other hydrological variables, because the climate system responds slowly to diverging greenhouse-gas forcing. This is consistent with IPCC analyses showing that even by 2081–2100, multi-model precipitation changes exhibit large internal variability, and scenario-specific signals (including between RCP4.5 and RCP8.5) often remain within one standard deviation of natural variability over many regions, including the Mediterranean basin. The hazard model relies mainly on precipitation and evapotranspiration, two variables for which scenario differences are comparatively small and uncertain, thus its outputs naturally show limited divergence between RCPs (IPCC 2021).

Despite these limitations, the modelling confirms that ground-deformation hazards are likely to increase over both the near and long term, driven by the combined influence of projected changes in precipitation and evapotranspiration and the continuation of current groundwater-extraction patterns. Climate change thus emerges as an important amplifier of existing hydrogeological pressures, particularly in areas with a long history of subsidence. The approach, coupling RCP-based climatic projections, groundwater-withdrawal trends, and exposure–vulnerability metrics, enables a consistent comparison across metropolitan contexts with varying data availability and geological settings. Although intentionally conservative, the results provide meaningful indications of where and how deformation-related stresses may intensify.

Overall, subsidence-related impacts are projected to be especially pronounced in metropolitan areas such as Bologna and Florence, where increasing hazard levels intersect with high exposure–vulnerability conditions (Lenardón Sánchez et al. 2024). These cities show the largest expected growth in high-risk zones, pointing to the need for prioritised intervention and long-term adaptation planning. The findings underscore the importance of integrated groundwater-management strategies, climate-informed urban planning, and sustained displacement monitoring to mitigate the accelerating effects of climate-driven subsidence on critical infrastructure and urban resilience.

5 REFERENCES

Arpae Emilia-Romagna (2026) Proiezioni climatiche in Emilia-Romagna. https://www.arpae.it/it/temi-ambientali/clima/previsioni-e-proiezioni/proiezioni-climatiche/proiezioni-climatiche-in-emilia-romagna. Accessed 17 Mar 2026

Cigna F, Paranunzio R, Bonì R, Teatini P (2025) Present-day land subsidence risk in the metropolitan cities of Italy. Sci Rep 15:. https://doi.org/10.1038/s41598-025-18941-8

Cigna F, Tapete D (2021) Present-day land subsidence rates, surface faulting hazard and risk in Mexico City with 2014–2020 Sentinel-1 IW InSAR. Remote Sens Environ 253:112161. https://doi.org/10.1016/j.rse.2020.112161

Collados-Lara AJ, Pulido-Velazquez D, Pardo-Igúzquiza E (2018) An integrated statistical method to generate potential future climate scenarios to analyse droughts. Water (Switzerland) 10:. https://doi.org/10.3390/w10091224

Cornes RC, van der Schrier G, van den Besselaar EJM, Jones PD (2018) An Ensemble Version of the E-OBS Temperature and Precipitation Data Sets. Journal of Geophysical Research: Atmospheres 123:9391–9409. https://doi.org/10.1029/2017JD028200

Jacob D, Petersen J, Eggert B, et al (2014) EURO-CORDEX: New high-resolution climate change projections for European impact research. Reg Environ Change 14:563–578. https://doi.org/10.1007/s10113-013-0499-2

Skempton AWK, Macdonald DH (1956) THE ALLOWABLE SETTLEMENTS OF BUILDINGS. Proceedings of the Institution of Civil Engineers 5:727–768. https://doi.org/10.1680/ipeds.1956.12202

Tarquini S, Vinci S, Favalli M, et al (2012) Release of a 10-m-resolution DEM for the Italian territory: Comparison with global-coverage DEMs and anaglyph-mode exploration via the web. Comput Geosci 38:168–170. https://doi.org/10.1016/j.cageo.2011.04.018

Teutschbein C, Seibert J (2012) Bias correction of regional climate model simulations for hydrological climate-change impact studies: Review and evaluation of different methods. J Hydrol (Amst) 456–457:12–29. https://doi.org/10.1016/j.jhydrol.2012.05.052

van der Linden P, Mitchell JFB (2009) ENSEMBLES: Climate Change and its Impacts: Summary of research and results from the ENSEMBLES project. 160

IPCC (2021) Climate Change 2021: The Physical Science Basis. Contribution of Working Group I to the Sixth Assessment Report of the Intergovernmental Panel on Climate Change

Lenardón Sánchez M, Farías CA, Cigna F (2024) Multi-Decadal Land Subsidence Risk Assessment at Major Italian Cities by Integrating PSInSAR with Urban Vulnerability. Land 2024, Vol 13, Page 2103 13:2103. https://doi.org/10.3390/LAND13122103